Chapter 2

# Supercontinuum Generation With Photonic Crystal Fibers and Its Application in Nano-imaging

Shuanglong Liu, Wei Liu and Hanben Niu

Additional information is available at the end of the chapter

http://dx.doi.org/10.5772/59987

## 1. Introduction

Supercontinuum (SC) generation describes the phenomenon that the output spectrum becomes much wider than the input spectrum when an ultrashort optical pulse passes through a nonlinear medium, such as bulk fused silica, photonic crystal fiber and so on. Since this phenomenon was first discovered by Alfano and Shapiroin in 1970s by passing picosecond pulses through a bulk BK7 glass [1], it has been explored in a wide variety of nonlinear media, including solids, gas, inorganic liquids and various waveguides.

In 1974, an ingenious idea of introducing microstructures into traditional step index optical fibers to modify the guidance properties by Kaiser and Altle [2] established the theoretical foundation for photonic crystal fiber (PCF). And the exploration for fabricating such fibers were never stopped until the advent of an all-silica PCF in Southampton University by Russell and co-workers in 1996 [3]. His birth drew much more interest from various scientific researchers and initiated a revolution in SC generation.

The PCF used for SC generation often has a solid core surrounded by regularly arranged microscopic air holes running along the fiber length [4], resulting in a surrounding region with lower refractive index compared to that of the central district. Therefore the light will be trapped and guided in the fiber core through total internal reflection. This modified surrounding shows good flexibility to engineer the waveguide properties. It is reported that the zero-dispersion wavelength (ZDW) in fused silica can shift to a shorter wavelength than the intrinsic ZDW about 1300 nm by suitable design of the air hole diameter and air filling fraction [5]. Then Ranka *et al.* first reported that the PCF can exhibit anomalous dispersion at visible region [6]. And they obtained an ultrabroadband continuum generation from 400 nm to 1600 nm by injecting a femtosecond pulse into a 75 cm section PCF. In 2000, Wadsworth *et al.* observed soliton effects by pumping a short PCF near the ZDW in the anomalous regime [7]. Accom-

panied with other nonlinear effects, the fundamental and second soliton were identified. The phenomenon of soliton self-frequency shift [8] in a tapered air–silica microstructure fiber was reported by Liu *et al.* from 1.3 to 1.65 μm. Numerical modeling of pulse evolution in PCFs was first proposed by Husakou and Herrmann [9] based on reduced Maxwell equations. And the important roles of soliton fission, four-wave mixing in spectral broadening were first discussed in detail. Due to the lack of Raman scattering, much fine structure was lost in the solution. An extended nonlinear Schrödinger equation (NLSE) was first applied to the modeling of femtosecond pulse propagation in PCF [10] with higher-order dispersion, self-steepening and Raman effects included. The numerical simulations based on extended NLSE is accurately consistent with experimental results. Based on the previous works, Genty *et al.* quantitatively studied the mechanisms of SC generation when the PCF was pumped in its normal and anomalous regimes [11]. Soon afterwards, continuum generation from 1065 to 1375 nm was demonstrated by pumping a honey fiber with continuous wave [12]. These numerical and experimental studies led to a detailed description of the SC generation in PCFs from the ultraviolet to the infrared in both femtosecond, picosecond regimes and continuous wave.

SC generation in PCFs involves several nonlinear effects such as self-phase modulation, (SPM) cross-phase modulation (XPM), self-steepening and optical shock formation, Raman scattering, solition fission, four-wave mixing and so on. Greatest spectral broadening was reported when a PCF was pumped in the anomalous dispersion regime near the ZDW [13]. The broadening mechanism in this case is dominated by soliton dynamics, especially breakup of higher-order solitons into fundamental solitons and non-solitonic radiation, though the SPM effect in initial propagation. The ejected solitons will shifts toward longer wavelength under intrapulse Raman scattering, known as soliton self-frequency shift (SSFS). Spectral broadening in normal dispersion region is mainly due to SPM effect and optical wave breaking. With soliton dynamics suppressed in this region, the generated SC possesses a good temporal structure in spite of a smaller spectral broadening. Under specific pump pulses, continua with broad spectral bandwidth, good spatial coherence, uniform intensity profile and simple temporal structure can be generated in certain PCFs. These continua show significant applications in many fields such as optical frequency metrology, optical communication and cellular biology.

Recent years have seen the fast development of cellular biology based on optical microscope and coherent lasers. And many microscopies were developed to observe the fine structures inside biologic cells, such as scanning electron microscope [14] (SEM), scanning tunneling microscope [15] (STM), and atomic-force microscope [16] (AFM). Though they all have very high spatial resolutions, vacuum circumstance needed in SEM makes it not suit for live-cell imaging while STM and AFM are restricted to surface mapping due to the cantilever tip [17]. With the development of several novel microscopic methods, such as photo-activated localization microscopy [18] (PALM), stochastic optical reconstruction microscopy [19] (STORM), stimulated emission depletion [20] (STED) microscopy, fluorescence microscopies obtain a spatial resolution about 20 nm and are widely used in cellular biology. But photo-toxicity, photo-bleaching and influence of invasive marker on cells cannot be ignored in vivo imaging, let alone some biomolecule that are difficult to be labeled [21]. Therefore it is urgent to develop

a microscopy with nano-scaled resolution to study the process of metabolism in live cells and its response to invasive substances.

As a new kind of microscopies based on molecular vibrations, coherent anti-Stokes Raman scattering (CARS) microscopy has exhibited their prospective applications in live-cell imaging for its distinct characteristics, including high sensitivity and spatial resolution, label-free chemical specificity, three-dimension sectioning capability [22-24]. In traditional CARS microscopy, the pump and Stokes pulses can resonant only single or few molecular bonds due to the limitation of the spectral bandwidth. Obviously it is not adequate to acquire accurate recognition and mapping of an unknown biomolecule or that with complex components. Although this can be achieved by sequentially tuning the frequency difference of them or synchronizing two ultrashort lasers, it is time-consuming and costs a lot. When a SC pulse generated in a high nonlinear PCF serves as both the pump the Stokes, most distinct vibration modes, perhaps full modes even, can be probed simultaneously as long as different frequency components in the generated SC propagate at about a same speed. And a method named additional probe-beam-induced phonon depletion [25] (APIPD) is proposed to improve the spatial resolution on CARS microscopy. In APIPD method, an additional doughnut beam with different frequency from that of the probe beam is introduced to deplete the phonons on the periphery of point spread function (PSF). The subsequent Gaussian probe beam reacts with the rest phonons, generating an anti-Stokes signal near centre of the PSF. By filtering out the signal induced by doughnut beam, the effective PSF is hence decreased, meaning a higher spatial resolution. And the resolution can be reduced below 100 nm by properly modifying the probe and additional probe beam. These characters make CARS microscopy especially suit for studying the process of metabolism in live cells.

In the latest 10 years, infrared (IR) microscope has been widely used in many industries, such as material analysis and cellular biology, for its ability of nondestructive imaging and molecular location based on vibrational spectroscopy [26,27]. Traditional IR microscopes are based on either thermal IR sources [28] with low brightness and coherence, such as a globar or Hg-lamp, or synchrotron radiation [29,30]. The synchrotron radiation is complex, expensive, power consuming and always accompanied with intensity fluctuation in spite of high brightness and coherence. The application of non-silica fibers [31-33] brings about a new IR source with both high brightness and coherence, not to mention the broad bandwidth.

In this chapter, the generalized nonlinear Schrödinger equation is briefly deduced, based on the Maxwell's equations. It takes not only the higher-order dispersion into consideration, but also the higher-order nonlinear effects including self-steepening, optical shock formation and intrapulse Raman scattering. Then a predictor-corrector split-step Fourier method is used to simulate the pulse evolutions in both temporal and spectral domain for its high accuracy and fast calculating speed. Based on the fiber structure, the dispersion parameters and nonlinear coefficient can be calculated with finite element method. Then the process of continuum generation in a PCF is described in detail, including pulse evolutions in both temporal and spectral domain. The generated SC has important applications in nonlinear optics, especially CARS microscopy and IR microscopy. Based on the vibrational spectroscopy, CARS microscopy and IR microscopy has been widely used in cellular biology for their label-free and

nondestructive imaging. In terms of the limited spatial resolution in CARS microscopy, an APIPD is proposed to break the diffraction barrier, leading to nano-scaled imaging. Furthermore, the combination of this CARS nanoscopy and the broadband continuum is of crucial importance to study the fine structures and metabolic dynamics in live cells. Besides, based on the atomic force microscope, FTIR microscopy has realized a spatial resolution below 100nm. Serving a mid-infrared supercontinuum generated with the chalcogenide PCF as pumping source, this nano-FTIR will become a powerful tool for chemical identification of unknown nanostructures.

## 2. Numerical modeling of supercontinuum generation

### 2.1. Nonlinear propagation equation

The propagation equation describing evolution of laser pulses in optical fibers could be derived from Maxwell's equations [34]

$$\nabla \times \mathbf{E} = -\frac{\partial \mathbf{B}}{\partial t}, \quad \nabla \times \mathbf{H} = \mathbf{J} + \frac{\partial \mathbf{D}}{\partial t}, \quad \nabla \bullet \mathbf{D} = \varrho_f, \quad \nabla \bullet \mathbf{B} = 0 \tag{1}$$

where **E** and **B** are electric field vector and magnetic flux density, **H** and **D** are magnetic field vector and electric flux density respectively. **J** and $\varrho_f$ are current density vector and free charge density. They could be related to themselves through the constitutive relations given by

$$\mathbf{D} = \varepsilon_0 \mathbf{E} + \mathbf{P}, \quad \mathbf{B} = \mu_0 \mathbf{H} + \mathbf{M} \tag{2}$$

where $\varepsilon_0$ and $\mu_0$ are vacuum permittivity and permeability, **P** and **M** are the induced electric and magnetic polarizations respectively. In optical fibers, **J**, $\varrho_f$ and **M** all equal to zero, for they are nonmagnetic and absent of free charges.

Based on the Maxwell's equations and constitutive relations, wave equation describing light propagation in optical fibers will be

$$\nabla^2 \mathbf{E} - \frac{1}{c^2}\frac{\partial^2 \mathbf{E}}{\partial t^2} = \mu_0 \frac{\partial^2 \mathbf{P}}{\partial t^2} \tag{3}$$

The induced electric polarization **P** , which in essence expresses the interaction between light and medium, will depend on the electric field strength as

$$\mathbf{P} = \varepsilon_0 [\chi^{(1)} \bullet \mathbf{E} + \chi^{(2)} : \mathbf{EE} + \chi^{(3)} \vdots \mathbf{EEE} + \ldots] \tag{4}$$

where $\chi^{(k)}$(k=1,2, 3, ...) is the k-order susceptibility. The linear susceptibility $\chi^{(1)}$ often contributes to the refractive index and fiber loss, while the second order susceptibility $\chi^{(2)}$ are related to the second order nonlinearity effects such as second

http://dx.doi.org/10.5772/59987

harmonic generation (SHG), sum frequency generation (SFG). The third order susceptibility $\chi^{(3)}$ is ofter accompanied by third harmonic generation (THG), four wave mixing (FWM) and so on. The second order susceptibility will be zero, because the fiber is Circular symmetric. So the induced electric polarization is

$$\mathbf{P} = \varepsilon_0[\chi^{(1)} \bullet \mathbf{E} + \chi^{(3)} \vdots \mathbf{EEE} + ...] \tag{5}$$

Also the induced electric polarization can be divided into two parts, the linear component $\mathbf{P}_L$ and nonlinear component $\mathbf{P}_{NL}$ given by $P_L = \varepsilon_0 \chi^{(1)} \bullet \mathbf{E}$, $P_{NL} = \chi^{(3)} \vdots \mathbf{EEE}$. The relations between linear component, nonlinear component and electric field could expressed as

$$P_L = \varepsilon_0 \int_{-\infty}^{t} \chi^{(1)}(t - t') \bullet \mathbf{E}(r, t') dt' \tag{6}$$

$$\mathbf{P}_{NL} = \varepsilon_0 \int_{-\infty}^{t} dt_1 \int_{-\infty}^{t} dt_2 \int_{-\infty}^{t} dt_3 \int_{-\infty}^{t} \chi^{(3)}(t - t_1, t - t_2, t - t_3) \vdots \mathbf{E}(r, t_1)\mathbf{E}(r, t_2)\mathbf{E}(r, t_3) \tag{7}$$

So Eq. (3) can also be

$$\nabla^2 \mathbf{E} - \frac{1}{c^2}\frac{\partial^2 \mathbf{E}}{\partial t^2} = \mu_0 \frac{\partial^2 \mathbf{P}_L}{\partial t^2} + \mu_0 \frac{\partial^2 \mathbf{P}_{NL}}{\partial t^2} \tag{8}$$

Before solving Eq. (8), some assumptions should be made to simplify it. First $\mathbf{P}_{NL}$ will be treated as a small perturbation to $\mathbf{P}_L$, because the nonlinear changes in the refractive index is very small, less than $10^{-6}$ in fact. Then the input pulse will keep its polarization when it travels in an optical fiber, to ensure the scalar approximation reasonable. At last, the input field is treated as a quasi-monochromatic light, which is justified when the pulse duration is more than 100 fs.

Supposing the third order susceptibility $\chi^{(3)}$ has the following form

$$\chi^{(3)}(t - t_1, t - t_2, t - t_3) = \chi^{(3)} R(t - t_1)\delta(t - t_2)\delta(t - t_3) \tag{9}$$

with $R(t)$ being the nonlinear resoponse function that has been normalized. So the nonlinear induced electric polarization is

$$\mathbf{P}_{NL} = \varepsilon_0 \chi^{(3)} \mathbf{E}(r, t) \int_{-\infty}^{t} R(t - t_1) |\mathbf{E}(r, t_1)|^2 dt_1 \tag{10}$$

Considering above equations, the numerical equation describing evolution of an optical pulse when it travels in a single-mode fiber is

$$\frac{\partial A}{\partial z} + \frac{\alpha A}{2} - \sum_{k \geq 2} \frac{i^{k+1}}{k!} \beta_k \frac{\partial^k A}{\partial T^k} = i\gamma\left(1 + i\tau_{shock}\frac{\partial}{\partial T}\right)\left[A \int_{-\infty}^{+\infty} R(T') \times |A(T - T')|^2 dt'\right] \tag{11}$$

This equation is known as the generalized nonlinear Schrödinger equation (NLSE). In Eq. (11), the left side models linear propagation effects, with A being the pulse envelope variation in a retarded time frame, $\alpha$ the fiber loss and $\beta_k$ the k-th order Taylor series expansion of mode propagation constant around the center frequency $\omega_0$ as

$$\beta(\omega)=\beta_0+\beta_1(\omega-\omega_0)+\frac{1}{2}\beta_2(\omega-\omega_0)^2+\ldots \tag{12}$$

The right side of Eq. (11) describes the nonlinear effects, such as self-steepening, Raman scattering, etc. with $\gamma$ being the nonlinear coefficient expressed as $\gamma(\omega_0)=n_2(\omega_0)\omega_0/cA_{eff}$, where $n_2$ is nonlinear refractive index, c is the speed of light in vacuum, $A_{eff}$ is effective mode area defined as $A_{eff}=\left(\iint |F(x,y)|^2dxdy\right)^2/\iint |F(x,y)|^4dxdy$. Here, $F(x,y)$ is the modal distribution for the fundamental fiber mode. The term of $\tau_{shock}$ derives from the frequency dependence of the effective mode area $A_{eff}$ and effective index $n_{eff}$, associated with effects such as self – steepening and optical shock formation. The relation of the time derivative term $\tau_{shock}$ and effective mode area $A_{eff}$, effective index $n_{eff}$ can be expressed as [35,36]

$$\tau_{shock}=\frac{1}{\omega_0}-\left[\frac{1}{n_{eff}(\omega)}\frac{\partial}{\partial\omega}n_{eff}(\omega)\right]_{\omega=\omega_0}-\left[\frac{1}{A_{eff}(\omega)}\frac{\partial}{\partial\omega}A_{eff}(\omega)\right]_{\omega=\omega_0} \tag{13}$$

In Eq. (13), $\tau_{shock}$ could approximately equal to $1/\omega_0$ when the spectral broadening is limited to 20 THz. While the spectral broadening increases to 100 THz or more, the second and third term should be taken into account [37].

R(t) is the nonlinear response function with both the electronic and nuclear contributions included. Since the electronic contribution is nearly instantaneous comparing to the nuclear contribution, R(t) could be written as [38-40]

$$R(t)=(1-f_R)\delta(t-t_e)+f_Rh_R(t) \tag{14}$$

with $f_R$ the fractional contribution of the delayed Raman response to nonlinear polarization, $t_e$ the short delay in electronic response, $h_R(t)$ the Raman response function. Often $t_e$ is very shot (<1 fs) that it could be neglected. So the nonlinear response function will be $R(t)=(1-f_R)\delta(t)+f_Rh_R(t)$. The Raman response function has different forms for fibers made of different materials. For silica fibers, a useful form of Raman response function will be [35]

$$h_R(t)=\left(\tau_1^2+\tau_2^2\right)\exp\left(-\frac{t}{\tau_2}\right)sin\left(\frac{t}{\tau_1}\right)\Theta(t)\Big/\left(\tau_1\tau_1^2\right) \tag{15}$$

where $\tau_1$ and $\tau_2$ are two adjustable parameters, $\Theta(t)$ is Heaviside function. In a research in 1989, values of $\tau_1$=12.2 fs and $\tau_1$=32 fs were used to model the profile of Raman response, and the

result shows good fit to the actual Raman-gain spectrum of silica fiber [35]. Based the peak Raman gain, the Raman response factor could be calculated, saying about 0.18 [38].

In Eq. (15), single Lorentzian profile was used to approximate the actual Raman gain spectrum which is widely used in investigating ultrafast nonlinear process in optical fibers for its simplicity. However, this model underestimates Raman gain below 10THz, while overestimating it beyond 15THz, making the Raman induced frequency shift not so accurate. To address this issue, another model of approximating nonlinear response function was proposed as [41]

$$R(t)=(1-f_R)\delta(t)+f_R[(f_a+f_c)h_a(t)+f_b h_b(t)] \tag{16}$$

with $f_a$=0.75, $f_b$=0.21, $f_c$=0.04, where $h_a(t)$ and $h_b(t)$ have the following forms

$$h_a(t)=(\tau_1^2+\tau_2^2)\exp\left(-\frac{t}{\tau_2}\right)sin\left(\frac{t}{\tau_1}\right)\Big/(\tau_1\tau_1^2) \tag{17}$$

$$h_b(t)=\frac{2\tau_3-t}{\tau_3^2}\exp\left(-\frac{t}{\tau_3}\right) \tag{18}$$

when the parameters are $\tau_1$=12.2 fs, $\tau_2$=32 fs, $\tau_3$=96 fs and $f_R$=0.245, the simulated Raman gain curve matchs the actual Raman gain profile very well in the whole range of 0-15 THz. To make the investigation more approximate to actual Raman response, a more accurate model could be used although it has more complicated forms [42].

### 2.2. Frequency-resolved optical gating

In this chapter, we will use the predictor-corrector SSFM proposed by Lee et.al [43] to simulate evolutions of pulses in time and frequency domain. This method shows both fast calculation speed and accurate numerical results. Also the cross-correlation frequency-resolved optical gating method [44-46] (XFROG) is employed to characterize the intensity and phase profiles of the generated continuum. The method describes the pulse structure simultaneously in the time and frequency domain which is intuitive for understanding the dynamics in continuum generation.

In measurement of a continuum based on XFROG, the continuum pulse and a reference pulse should be focused on a nonlinear crystal to generate a sum-frequency signal (SFG signal) after being synchronized in the time domain by a time delay system as shown in figure 1(b). The generated SFG signals under different delay times will be recorded by a spectrometer, with which the XFROG trace could be retrieved. The XFROG trace is

$$I_{XFORG}(\omega,\tau)=\left|\int_{-\infty}^{+\infty}E_{sig}(t,\tau)exp(-i\omega t)dt\right|^2 \tag{19}$$

with the SFG signal field $E_{sig}(t,\tau) = E(T)R(T-\tau)$ where $E(T)$ is the optical field of a continuum which needs to be measured, $R(T-\tau)$ the optical field of reference pulse who has a delay time $\tau$ compared to the reference pulse.

It is critical to measure the reference pulse first, because its intensity and phase information will be used to retrieve the continuum pulse. For measurement of a continuum generated in a photonic crystal fiber, the pumping pulse is usually selected to be the reference pulse, although the reference pulse could be any pulse. In measurement of the reference pulse, it will be split into two beams, one as a new pulse to be measured and another as a new reference pulse as shown in figure 1(a). The two beams are focused on the nonlinear crystal to generate a SFG signal that will be measured by the spectrometer. So the FROG trace will be

$$I_{FORG}(\omega,\tau) = \left|\int_{-\infty}^{+\infty} E(T)E(T-\tau)exp(-i\omega t)\,dt\right|^2 \quad (20)$$

Since the measuring pulse and reference pulse have the same intensity and phase profiles, this FROG is often called self-correlation FROG [47,48].

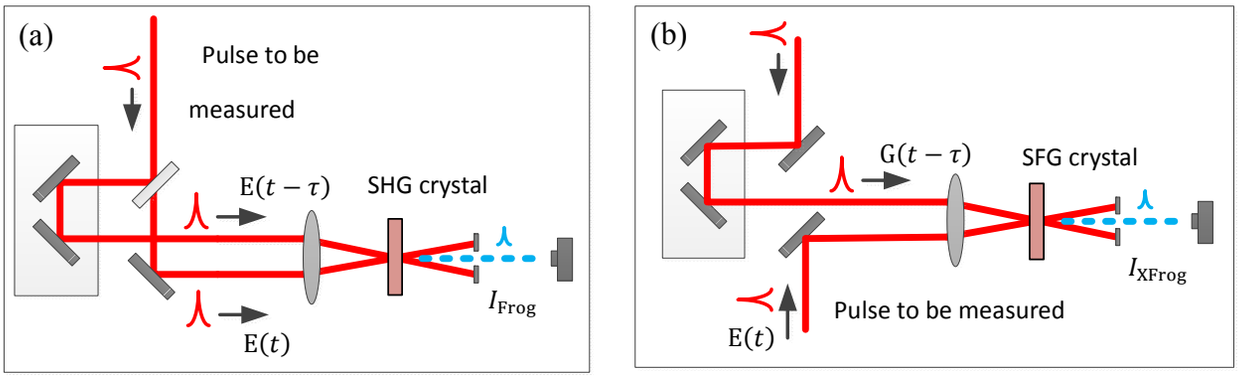


**Figure 1.** Schematic of (a) auto-correlation FROG and (b) cross-correlation FROG

Fig.1 Schematic of (a) auto-correlation FROG and (b) cross-correlation FROG

### 2.3. Basic numerical results

## 2.3 Basic numerical results

*2.3.1. Calculation of dispersive parameters*

### 2.3.1 Calculation of dispersive parameters

The bound electrons in medium acts as forced vibration when an optical wave passes through the medium. This interaction often manifests as variation of refraction index, in which the real parts describe the dispersion characteristic and the imaginary parts accounts for absorption of the input wave. When the frequency of input field is away from the resonant frequency, the refraction index could well approximate by the Sellmeier equation [49]

$$n^2(\omega) = 1 + \sum_{j=1}^{m} \frac{B_j \omega_j^2}{\omega_j^2 - \omega^2} \quad (21)$$

where $\omega_j$ and $B_j$ are the j-th resonant frequency and strength. The parameters $\omega_j$ and $B_j$ will change with different core constituents [50]. For bulk-fused silica, the following values of $\omega_j$ and $B_j$ are used to fitting the real dispersion curves [51]

http://dx.doi.org/10.5772/59987

where $\omega_j$ and $B_j$ are the j-th resonant frequency and strength. The parameters $\omega_j$ and $B_j$ will change with different core constituents [50]. For bulk-fused silica, the following values of $\omega_j$ and $B_j$ are used to fitting the real dispersion curves [51]

$$B_1=0.6961663,\quad \lambda_1=0.0684043\ \mu m$$
$$B_2=0.4079426,\quad \lambda_2=0.1162414\ \mu m$$
$$B_3=0.8974794,\quad \lambda_3=9.8961610\ \mu m$$

The variation of refractive index and dispersion parameter for fused silica with wavelengths are shown in figure 2 with $n$ being the refractive index and $n_g$ being the group index. Group index $n_g$ decreases with wavelength below about $1.31\ \mu m$ and increases beyond that wavelength point. For this reason, the region below $1.31\ \mu m$ is often called anomalously dispersive region, with the other one being anomalously dispersive region. Also the demarcation point between normal and anomalous regimes is known as zero-dispersion wavelength (ZDW).

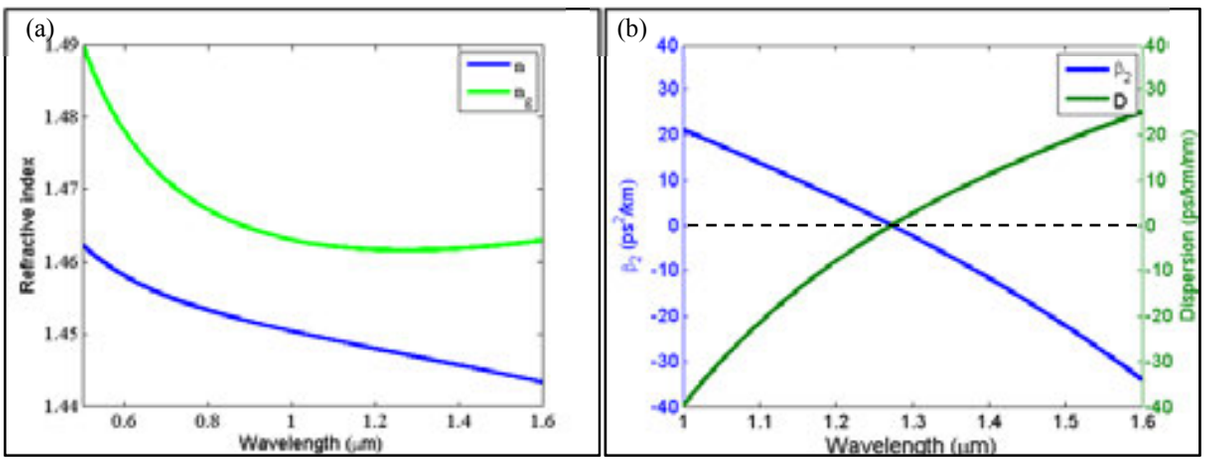


Fig.2 (a) variation of refractive index $n$ and group index $n_g$ with wavelength for fused silica and (b) variation of group-velocity dispersion $\beta_2$ and dispersion parameter D with wavelength in bulk fused silica

**Figure 2.** (a) variation of refractive index $n$ and group index $n_g$ with wavelength for fused silica and (b) variation of group-velocity dispersion $\beta_2$ and dispersion parameter D with wavelength in bulk fused silica

The dispersive effect in optical fibers is related to the Taylor series of mode propagation constant around the center frequency $\omega_0$

$$\beta(\omega)=n(\omega)\frac{\omega}{c}=\beta_0+\beta_1(\omega-\omega_0)+\frac{1}{2}\beta_2(\omega-\omega_0)^2+\cdots+\frac{1}{2}\beta_2(\omega-\omega_0)^2+\cdots \quad (22)$$

where c is velocity of light, $\beta_k$ is k-th dispersion coefficient expressed by

$$\beta_k=\left(\frac{\partial^k\beta(\omega)}{\partial\omega^k}\right)_{\omega=\omega_0} \qquad \beta_k=\left(\frac{\partial^k\beta(\omega)}{\partial\omega^k}\right)_{\omega=\omega_0} \quad (23)$$

The second dispersion coefficient $\beta_2$ accounts for the group velocity dispersion (GVD), mainly leading to pulse broadening. In fact, another dispersion parameter D is usually used to describe the dispersive effect.

The second dispersion coefficient $\beta_2$ accounts for the group velocity dispersion (GVD), mainly leading to pulse broadening. In fact, another dispersion parameter D is usually used to describe the dispersive effect.

$$D = -\frac{2\pi c}{\lambda^2}\beta_2 = -\frac{\lambda}{c}\frac{\partial^2 n}{\partial \lambda^2} \tag{24}$$

Dispersive effect in a PCF is associated with both the material dispersion and waveguide dispersion while it mainly arises from material dispersion in bulk materials. Therefore, in terms of dispersion in a PCF, the fiber structure and index distribution should be both taken into account. Considering a solid-core PCF made of fused silica, the finite element method (FEM) is used to model the fundamental mode distribution for different input wavelengths [52-54]. In the modeling, the air hole diameter $d$ and pitch $\Lambda$ are set to be 1.4 μm and 1.6 μm respectively [6], leading to the cross-section profile of the PCF as shown in figure 3(a). Figure 3(b) shows a two-dimension distribution of the fundamental mode for input wavelength $\lambda$=0.4 μm with the material dispersion included. Based on this simulation, the effective index of the PCF $n_{eff}$ is about 1.462353.

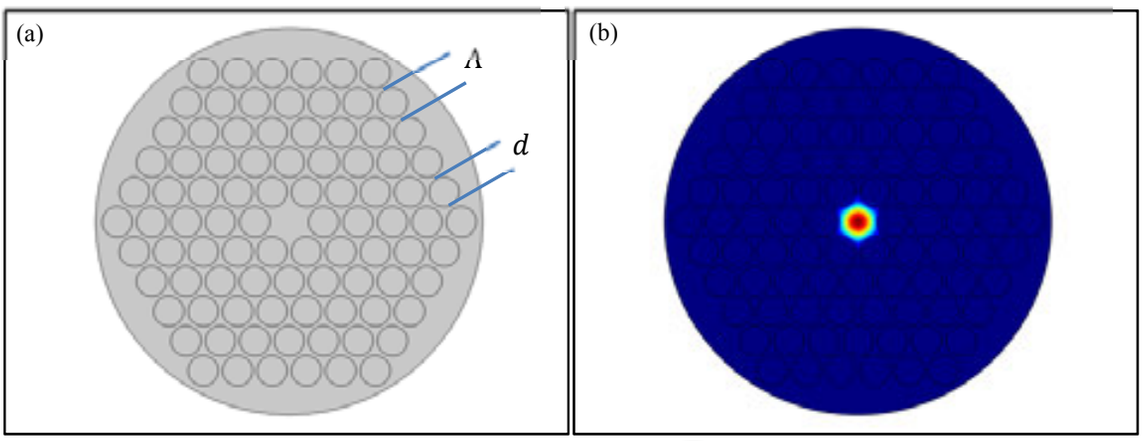


Fig.3 (a) Cross-section model of the PCF; (b) Two-dimension distribution of the fundamental mode

**Figure 3.** (a) Cross-section model of the PCF; (b) Two-dimension distribution of the fundamental mode

By calculating every $n_{eff}$ corresponding to different input wavelength, the variation of effective index with wavelength is fitted using MATLAB. Then the GVD parameter $\beta_2$ and dispersion parameter D are obtained with Eq. (24) and the profiles with wavelength are plotted in figure 4 respectively. Obviously the ZDW locates at about 730 nm and there is only one ZDW in the range from visible light to near-infrared.

By calculating every $n_{eff}$ corresponding to different input wavelength, the variation of effective index with wavelength is fitted using MATLAB. Then the GVD parameter $\beta_2$ and dispersion parameter D are obtained with Eq. (24) and the profiles with wavelength are plotted in figure 4 respectively. Obviously the ZDW locates at about 730 nm and there is only one ZDW in the range from visible light to near-infrared.

*2.3.2. SC generation with PCF*

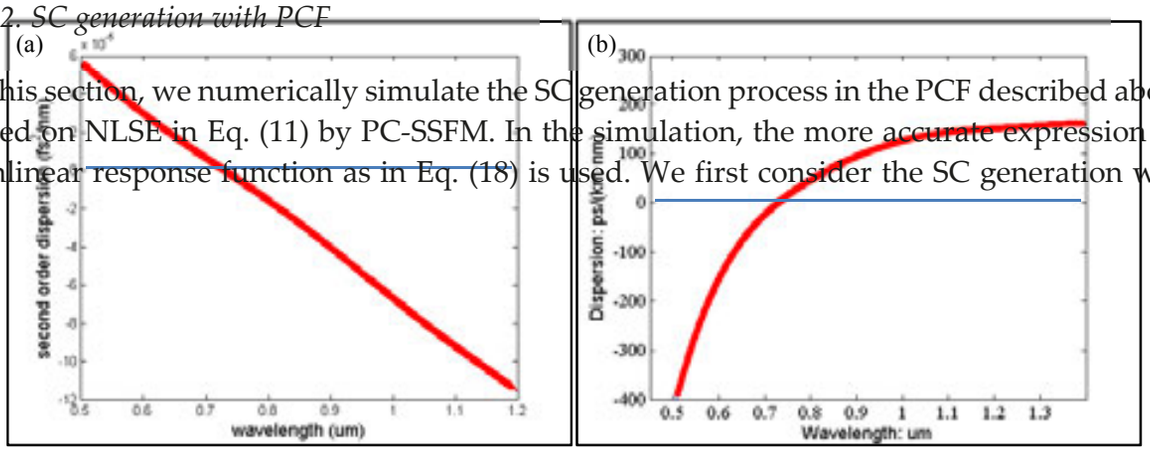


In this section, we numerically simulate the SC generation process in the PCF described above based on NLSE in Eq. (11) by PC-SSFM. In the simulation, the more accurate expression for nonlinear response function as in Eq. (18) is used. We first consider the SC generation with

effective index with wavelength is fitted using MATLAB. Then the GVD parameter $\beta_2$ and dispersion parameter D are obtained with Eq. (24) and the profiles with wavelength are plotted in figure 4 respectively. Obviously the ZDW locates at about 730 nm, and there is only one ZDW in the range from visible light to near-infrared.


http://dx.doi.org/10.5772/59987

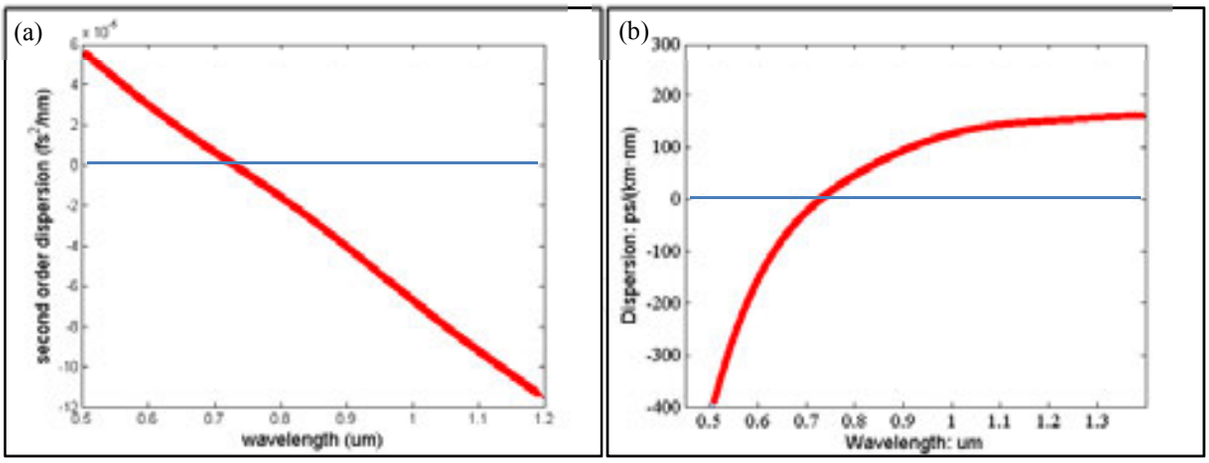


Fig.4 Variation of GVD parameter$\beta_2$ (a) and dispersion parameter D (b) with wavelength

**Figure 4.** Variation of GVD parameter $\beta_2$ (a) and dispersion parameter D (b) with wavelength

### 2.3.2 SC generation with PCF

In this section, we numerically simulate the SC generation process in the PCF described above based on NLSE in Eq. (11) by the SSFM. In the simulation, the more accurate expression for nonlinear response function as in Eq. (18) is used. We first consider the SC generation with PCF described above with hole diameter 1.4 μm and hole pitch 1.6 μm. Because of the ZDW about 730 nm, pump pulses with central wavelength of 800 nm are used to launch the fiber where the nonlinear parameter is estimated to be$0.113\,\mathrm{W^{-1}m^{-1}}$ . And the Taylor series expansion coefficients are $\beta_2 = -1.581\times10^{-5}\mathrm{fs}^2/\mathrm{nm}$、$\beta_3 = 7.819\times10^{-5}\mathrm{fs}^3/\mathrm{nm}$、$\beta_4 = -1.015\times10^{-4}\mathrm{fs}^4/\mathrm{nm}$、$\beta_5 = 2.549\times10^{-4}\mathrm{fs}^5/\mathrm{nm}$、$\beta_6 = -4.808\times10^{-6}\mathrm{fs}^6/\mathrm{nm}$.

Assume the initial input pulse has a hyperbolic scant profile that could be expressed as

$$A(0,t) = \sqrt{P}\,\mathrm{sech}\left(\frac{t}{t_0}\right)\exp\left(-\frac{iCt^2}{2t_0^2}\right) \quad (25)$$

with$P$ being the peak power, $t_0$ the pulse duration at $1/e$-intensity point, $C$ the initial chirp parameter. It is worth noting that the full width at half maximum (FWHM) is $2\ln\left(1+\sqrt{2}\right)$ times as large as$t_0$ . In this simulation, the peak power and pulse duration are set as $P = 10$ kW , $t_{FWHM} = 50$ fs, neglecting the initial chirp.

The temporal and spectral evolutions of input pulse with propagation distance are depicted in figure 5. In the initial stage of propagation, the spectral broadening is almost symmetric. And the short wavelength edge of the spectrum is steepened, whereas the long edge is pressed strongly. After that, the spectral broadening becomes strong asymmetric with distinct peaks on the long and short wavelength sides. The long wavelength components manifest the breakup of input pulse into several sub-pulses, known as soliton fission [52] caused by high-order dispersion and self-steepening effects of input pulse with propagation distance. The peaks nents are related to SPM effect and dispersion wave generation [55,56].

With longer propagation, the SC shows larger spectral broadening mainly on the long wavelength side due to soliton self-frequency shift (SSFS) induced by stimulated Raman scattering, while the spectral broadening on the short wavelength side almost remains unchanged. The spectral broadening process is often accompanied with re-distribution of

short wavelength sides. The long wavelength components manifest the breakup of input pulse into several sub-pulses, known as soliton fission[52] caused by high-order dispersion, self-steepening effect and Raman scattering. The short wavelength components are related to SPM effect and dispersion wave generation[55,56].

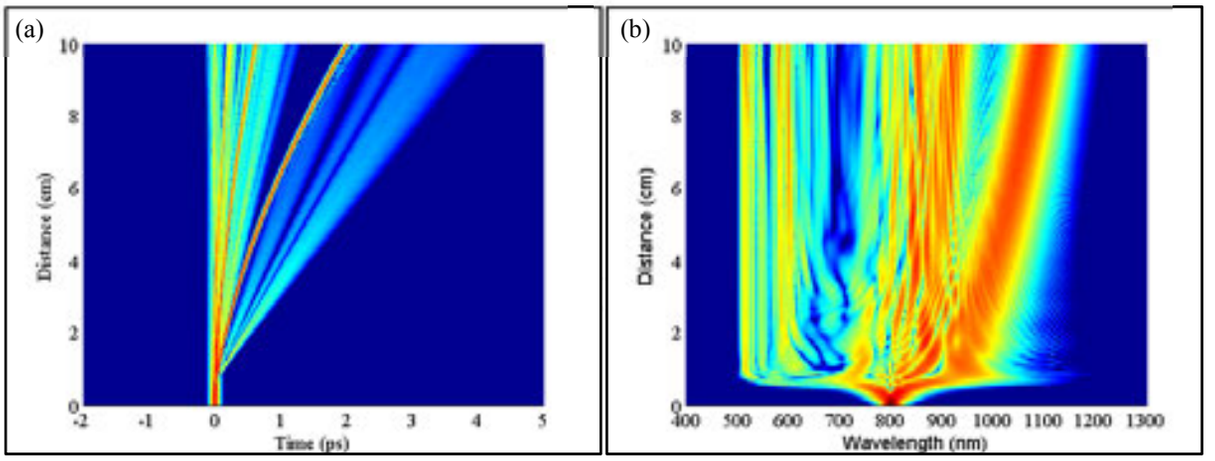


Fig.5 Temporal (left) and spectral (right) evolution over a propagation distance for input pulse centered at 800 nm with peak power 10kW and pulse duration 50fs

**Figure 5.** Temporal (left) and spectral (right) evolution over a propagation distance for input pulse centered at 800 nm with peak power 10kW and pulse duration 50fs

With longer propagation, the SC shows larger spectral broadening mainly on the long wavelength side due to soliton self-frequency shift (SSFS) induced by stimulated Raman scattering, while the spectral broadening on the short wavelength side almost remains unchanged. The spectral broadening process is often accompanied with re-distribution of energy, that the long wavelength components possess more while the short wavelength components possess less. This is explained by that: With the blue-shift components as pumping light, Raman gain will amplify the red-shift components effectively, leading to energy's transferring from blue components to red components. This energy transfer describes the red shift of the soliton spectrum with propagation distance.

To study the detailed characteristics of the generated SC, temporal and spectral slices at 15 cm propagation distance are plotted in figure 6. The time structure and spectrum are both shown on a linear scale and the intensity is normalized. There are three main peaks in the time domain located at 0.46 ps, 1.2 ps, and 3.8 ps, corresponding to the distinct peaks at 870 nm, 953 nm, and 1143 nm respectively in the frequency domain. These three peaks are caused by soliton fission and their central positions in both time and frequency domain are determined by their intrinsic characteristics, SSFS effect and the propagation distance.

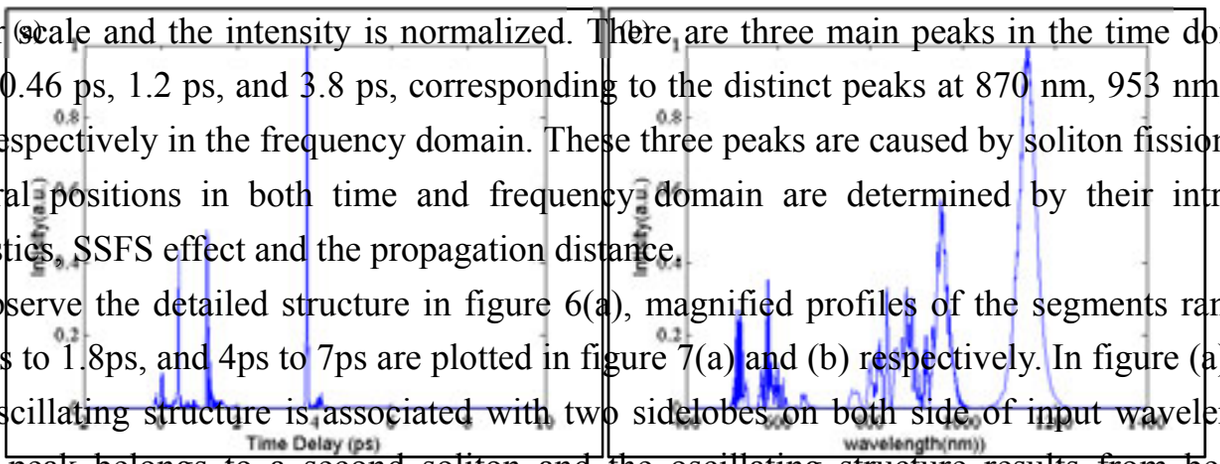


Fig.6 Pulse characteristics in (a) time and (b) frequency domain after 15 cm propagation

**Figure 6.** Pulse characteristics in (a) time and (b) frequency domain after 15 cm propagation

To observe the detailed structure in figure 6(a), magnified profiles of the segments ranging from 1.1 ps to 1.8ps, and 4ps to 7ps are plotted in figure 7(a) and (b) respectively. In figure (a), the ultrafast oscillating structure is associated with two sidelobes on both side of input wavelength. The main peak belongs to a second soliton and the oscillating structure results from beating between the two sidelobes. The relation of them is easy to see in figure 7(c) with 370 nm separation in spectrum at delay time 1.2 ps. There are still some fine oscillating structures lower than the two peaks in figure (a) ranging from 1.4 ps to 1.8 ps. There exists a little bump ranging from 4.6 ps to 6.5 ps in figure (a) with figure (b) being the magnification of partial structure. This bump is related to the dispersion wave generation around 546 nm.

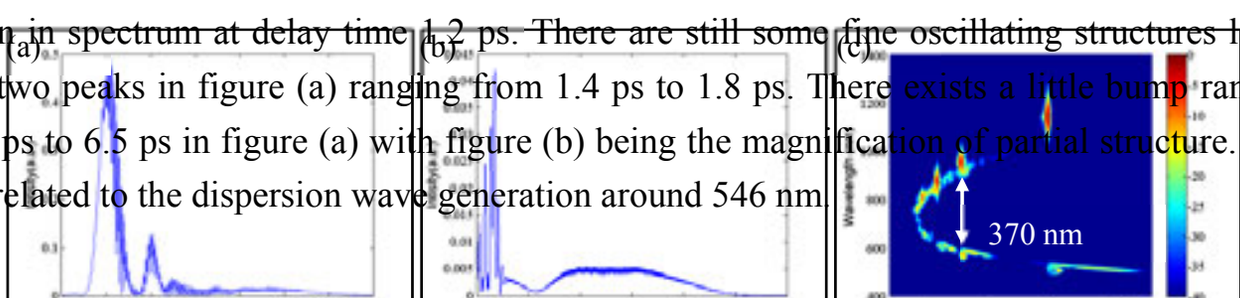

http://dx.doi.org/10.5772/59987

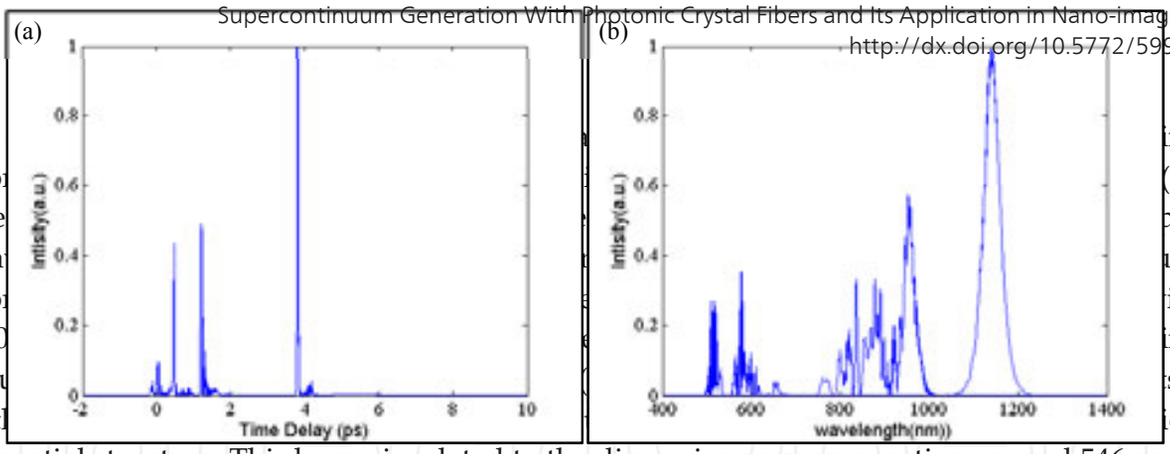


To ing
fro (a),
the ut
wa lts
fro ith
370 ing
stru s a
litt ion
of partial structure. This bump is related to the dispersion wave generation around 546 nm.

Fig.6 Pulse characteristics in (a) time and (b) frequency domain after 15 cm propagation

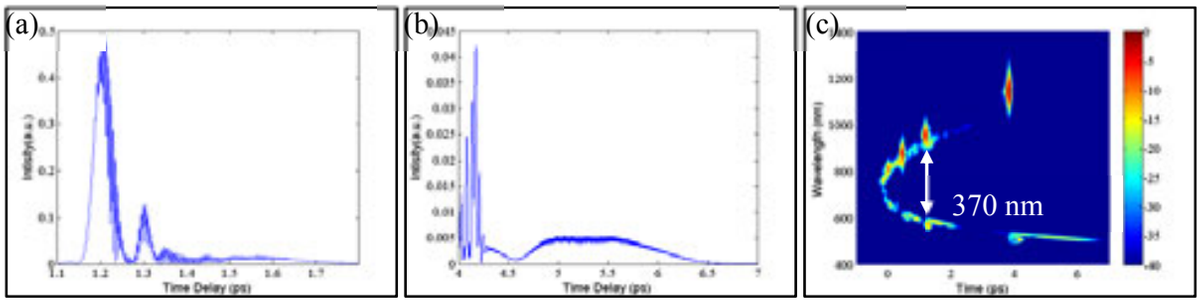


Fig.7 (a) Oscillating structure ranging from 1.2 ps to 1.7ps (b) Generated dispersion wave ranging from 4.6

**Figure 7.** (a) Oscillating structure ranging from 1.2 ps to 1.7ps (b) Generated dispersion wave ranging from 4.6 ps to 6.5 ps (c) Spectrogram with 15 cm propagation distance

ps to 6.5 ps (c) Spectrogram with 15 cm propagation distance

## 3 Supercontinuum used in coherent anti-Stokes Raman scattering nanoscopy

## 3. Supercontinuum used in coherent anti-Stokes Raman scattering nanoscopy

### 3.1 Theories of CARS process

### 3.1. Theories of CARS process

Coherent anti-stokes Raman scattering (CARS) has proven to be a promising nonlinear optical technique that is capable of obtaining high-sensitivity and three dimensional images based on molecular vibrational spectrum without labeling [57,58]. CARS is an example of a four-photon process. The first two light-matter interactions, one with pump frequency $\omega_L$ and another with Stokes frequency $\omega_S$, set up the state of vibrational resonance, a pump photon is annihilated, correspondingly a Stokes photon and a phonon (i.e., the energy quanta of the material excitation)is generated, the number of phonons is equal to the generated Stokes photons. The second light-matter interactions, the energy quanta of the material excitation, phonons, interact with the probe photons to generate a coherent anti-Stokes signal. In general, both processes occur simultaneously and the whole process can be treated as a four-photon process[59]. The detected signal strength depends nonlinearly on incident intensity.

Coherent anti-stokes Raman scattering (CARS) has proven to be a promising nonlinear optical technique that is capable of obtaining high-sensitivity and three dimensional images based on molecular vibrational spectrum without labeling [57,58]. CARS is an example of a four-photon process. The first two light-matter interactions, one with pump frequency $\omega_L$ and another with Stokes frequency $\omega_S$, set up the state of vibrational resonance, a pump photon is annihilated, correspondingly a Stokes photon and a phonon (i.e., the energy quanta of the material excitation)is generated, the number of phonons is equal to the generated Stokes photons. The second light-matter interactions, the energy quanta of the material excitation, phonons, interact with the probe photons to generate a coherent anti-Stokes signal. In general, both processes occur simultaneously and the whole process can be treated as a four-photon process [59]. The detected signal strength depends nonlinearly on incident intensity.

The full quantum picture of CARS process is depicted in Fig.8. $|e\rangle$ and $|g\rangle$ correspond to the vibration excited and ground state respectively. For simplicity of analysis, a single frequency model is provided. All laser fields-the pump, Stokes, probe, and phonons (or molecules) are quantized. The whole CARS process can be divided into two individual steps as shown in Fig.

The full quantum picture of CARS process is depicted in Fig 8 (A). $|e\rangle$and $|g\rangle$correspond to the vibration excited and ground state respectively. For simplicity of analysis, a single frequency model is provided. All laser fields-the pump, Stokes, probe, and phonons (or molecules) are quantized. The whole CARS process can be divided into two individual steps as shown in Fig.
8. In the first step, a coherent phonon population is directly created by coherent Raman scattering when a pump beam at frequency $\omega_L$ and a Stokes beam at frequency $\omega_S$ with frequency difference $\omega_L - \omega_S$ tuned to a Raman-active molecular vibration $\omega_v$ arrive at the sample simultaneously via a high numerical aperture objective. The process is impulsively stimulated

8. In the first step, a coherent phonon population is directly created by coherent Raman scattering when a pump beam at frequency $\omega_L$ and a Stokes beam at frequency $\omega_S$ with frequency difference $\omega_L - \omega_S$ tuned to a Raman-active molecular vibration $\omega_v$ arrive at the sample simultaneously via a high numerical aperture objective. The process is impulsively stimulated Raman scattering (ISRS), which is considered as the main mechanism of coherent phonon generation [60,61]. The coherent phonons are bosons and do not obey an exclusion principle. They are in a non-equilibrium state and in phase. In the second step, the coherent phonons interact with a time-delayed probe beam at frequency $\omega_P$ to generate a blue-shift anti-Stokes signal at $\omega_{AS} = \omega_P + \omega_v$, leading to separation of the CARS signal from the incident laser beams conveniently and efficiently rejecting fluorescence. Delay time between coherent phonons and probe beam is certainly much shorter than the vibrational dephasing time.

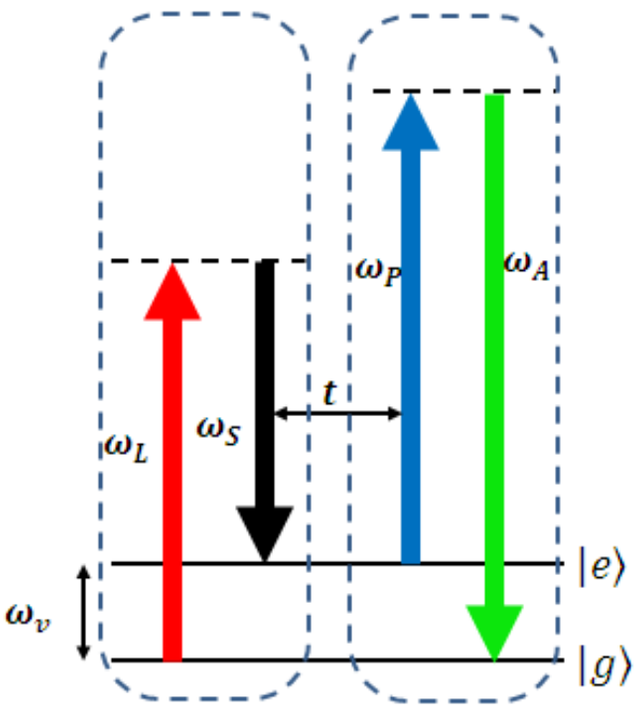


**Figure 8.** Energy level diagram of the two individual steps in CARS

The quantum mechanical treatment of the first process, which is a second-order process involving two light-matter interactions, resembles the spontaneous Raman effect. The important difference of the two is that in CARS process, the Stokes light stems from an applied laser field. Spontaneous Raman is a weak effect because the spontaneous interaction through the vacuum field occurs only rarely. This weakness can be overcome when the spontaneous nature of the initial state to final state $i \rightarrow f$ transition is eliminated by applying a second field of frequency $\omega_s$. The treatment is based on the calculation of the transition rate between the states of the molecule, which is described by Fermi's golden rule. The equation (26) predicts the growth of the generated Stokes photons, i.e., phonon number [62,63]

http://dx.doi.org/10.5772/59987

$$\frac{d n_S^{inc}}{dl} = N \bullet \frac{\pi e^4 \omega_L \ \omega_S}{2\varepsilon_0^2 \hbar^2 V^2 \mu_L^2 \ \mu_S c} \mid \alpha_R \mid^2 n_L^* \left[ n_S^* + 1 \right] \delta\left(\omega_S - \omega_L + \omega_v\right) \tag{26}$$

Consider a volume $V$ , which contains $N$ molecules and has a length $l$ parallel to the beam propagation direction. The Raman transition polarizability $\alpha_R$ plays a role similar to the classical polarizability change $(\partial\alpha / \partial q)$. $\omega_L$ and $\omega_S$ is the frequencies of pump and Stokes light, respectively. $e$ is the electron charge, $\varepsilon_0$ is the vacuum permittivity, $\hbar$ is Planck's constant, and $\delta$ is the Dirac delta function.$\mu_L$ and $\mu_S$ denote the refractive indexes. $n_S^{inc}$ indicates the increased (decreased) number of Stokes (pump) photons, i.e., the phonon number of energy $\hbar\omega_v$ , $n_{phonon}$. In the CARS process, the Stokes light stems from an applied laser field, and the $n_S^*$ consists of the applied Stokes photon $n_S$ and increased number $n_S^{inc}$ that stems from the first two light-matter interaction process. Similarly, $n_L^*$ , amounts to the pump photon number $n_L$ subtracting the decreased number $n_S^{inc}$. With the use of the pump and Stokes laser light sources of sufficiently high power, $n_S^{inc} \ll n_L$ , $n_S$ ,the present pump and Stokes number $n_L^* = n_L - n_S^{inc}$, $n_S^* = n_S + n_S^{inc}$, approximately amount to $n_L$ and $n_S$, and the factor 1 in equation (26) can be omitted at the same time. The laser intensities $I_L$ and $I_S$ exist on the focal plane in the form of Gaussian distribution, and we adopt an infinitesimal region in the focal plane where the intensities can be supposed constant $I_L = (\hbar \omega_L \ c / \mu_L \ V) n_L$ , $I_S = (\hbar \omega_S c / \mu_S V) n_S$. In an fs-CARS transient, the pump and Stokes beams temporally overlapped, coherently excite the molecular field, the duration of the transitory process denoted by the coherent excitation time is negligible. The homogeneous broadening of the atomic final state converts the delta function to a Lorentzian lineshape. when $\omega_S = \omega_L - \omega_v$, $\delta\left(\omega_S - \omega_L + \omega_v\right) \to \frac{\Gamma / \pi}{(\omega_S - \omega_L + \omega_v)^2 + \Gamma^2} = \frac{1}{\pi\Gamma}$, where $\Gamma$ denotes the linewidth relating to the dephasing time $T_2$ of the physical system, $\Gamma = 1 / T_2$.

Accordingly, from the equation (26), we obtain:

$$n_S^{inc} = \frac{I_S \mu_S V}{\hbar \omega_S \ c} \bullet I_L \ gl \tag{27}$$

where $g$ is the gain coefficient, $N_0$ is the molecule density.

$$g = N_0 \bullet \frac{e^4}{2\varepsilon_0^2 \hbar^3 V^2 \mu_L^2 \ \mu_S c^2} \frac{\omega_S}{\mu_L \ \mu_S} \mid \alpha_R \mid^2 \frac{1}{\Gamma} \tag{28}$$

Then, considering a molecule with just a single vibrational transition, the coherent phonon number per time unit in the first ISRS step can be written as

$$n_v = \frac{I_S \mu_S V}{\hbar \omega_S \ c} \bullet I_L \ gl \tag{29}$$

where $n_v$ indicates the coherent phonon number. The interaction volume V, which contains N molecules, is defined by the diffraction-limited focal spot area $A_{foc}$ and the interaction length $l$ paralleling to the beam propagation direction. For $g \propto N_0$ , it is apparent that the coherent phonon number is linearly dependent on $N_0$.

The phonon number subjects to a saturation effect and will not increase infinitely with the growth of incident light powers [64]. The maximum of coherent phonon number per pulse is molecule number in the focal volume. In another word, all of the molecules in the focus are excited to the vibrational state.

$$n_v^{pulse} = \frac{I_S \mu_S V}{\hbar \omega_S c} \bullet I_L \; g\tau \le N \tag{30}$$

Here, $n_v^{pulse}$ is the coherent phonon number per pulse. The magnitude of the spot is roughly estimated as $\sim 10^{-9}$ cm$^2$ , corresponding to a focal volume $V \sim 8 \times 10^{-14}$ cm$^3$. The gain coefficient is $g \sim N_0 \times 10^{-31}$cm/W. From equation (30), we see that saturation of coherent phonons results in product of the pump and Stokes intensities not exceeding $\sim 10^{18}$W$^2$/cm$^4$. Therefore in the first step of a T-CARS process, the pump and Stokes power density at focus is on the same order of $\sim 10^9$W/cm$^2$. In principle, if the pump and Stokes intensity exceed such an extreme value, the further increased intensity will not contribute to generation of the coherent phonons any more. In practice, however, energy of the pump and Stokes may be higher than that theoretical estimation due to the spectral broadening of femtosecond laser pulses.

Hereafter, we analyze the second step in CARS process. In the spontaneous Raman anti-Stokes process, the involved lattice vibrations called incoherent phonons are thermally excited with a density function $n_v$ given by the Bose-Einstein distribution. In this case, oscillatory phases of the phonons are completely random. Thus, individual oscillatory motions are canceled out by each other. Spontaneous Raman scattering is an incoherent linear process and the incoherent signal is randomly scattered to $4\pi$ solid angle, then the collected signal is [65]

$$P_A = N\left(\frac{\partial \sigma}{\partial \Omega}\right)_A n_v I_L \; \Omega_{collection} \tag{31}$$

with $P_A$ representing the anti-Stokes power, $I_L$ the incident laser intensity and $\Omega_{collection}$ the effective collection angle.$\left(\frac{\partial \sigma}{\partial \Omega}\right)_A$ is the spontaneous Raman differential scattering cross section. The scattered signal is proportional to the incident laser intensity and the occupation number of the upper Raman level. Different from spontaneous anti-Stokes Raman scattering, the second step in CARS is via introducing probe photons to interact with the coherent phonons, which are in a non-equilibrium state and in phase. Delay time between coherent phonons and probe beam is certainly much shorter than the vibrational dephasing time. Therefore, relaxation of the phonons is omitted, that is, all phonons are considered to have chances to interact with the probe photons and the impact of the delay time on the signal strength can be readily omitted. An important advantage of CARS microscopy over sponta-

neous Raman scattering microscopy is the fact that CARS signal is emitted into a $10^{-4}sr$ range, comparing to spontaneous Raman signal randomly scattered into $4\pi$ solid angle, which provides an important information that scattering cross section $\partial\sigma_C$ for the interaction of coherent phonons and probe photons is estimated to be enhanced by about five orders of magnitude [66]. In some sense, coherent process is equivalent to increasing the scattering cross section. The coherent anti-Stokes photons are confined to such a small solid angle, thus a condenser can almost completely collect the forward propagating signal. For low concentration samples, the distance between adjacent solute molecules is so great that energy of the coherent phonons cannot effectively transmit from one molecule to another. Accordingly, in the second step, the anti-Stokes signal strength is exclusively proportional to the number of coherent phonons and then linear dependence on the concentration of solute molecules. Comparing with incoherent (spherical) spontaneous Raman process, we calculate the number of the detected photons for coherent (directional) CARS in the repetition mode as

$$n_{CARS}^{low} = n_v^{pulse} \bullet n_P \bullet \frac{1}{A_{foc}} \partial\sigma_C \bullet \Delta t f_{rep} \tag{32}$$

In contrast, for high concentration samples, the coherent phonon energy can freely transmit among solute molecules in the focal volume, therefore in the second step, anti-Stokes signal strength isn't simply proportional to the coherent phonon number but also concerns with the molecule number. The overall T-CARS process depends quadratically on concentration, hence the anti-Stokes photon number in the repetition mode is

$$n_{CARS}^{high} = N \bullet n_v^{pulse} \bullet n_P \bullet \frac{1}{A_{foc}} \partial\sigma_C \bullet \Delta t f_{rep} \tag{33}$$

where, $n_{CARS}^{low}$ and $n_{CARS}^{high}$ denote anti-Stokes photon number in the low and high concentration samples, respectively. $n_P$ is photon number of the probe beam per pulse. The three pulsed near-infrared excitation beams are tightly focused with a 1.2NA water-dipping lens for deeper penetration depth to the spot area $A_{foc}$. $\Delta t$ is exposure time. $N$ is molecule number in the foci. In short, for $n_v^{pulse} \propto N_0$ , the anti-Stokes signal strength is strictly linear and quadratic on concentration in the low and high concentration samples, respectively, which conflicts with the popular statements of CARS signal consistently quadratic concentration dependence. The linear concentration dependence is especially beneficial to quantitative analysis for low concentration samples [67-70]. In the cross area between the low and high concentration, the observed concentration dependence from the relative experiments is neither quadratic nor linear, i.e., $n_{CARS} \propto N^{\alpha}$, where $1<\alpha<2$. An experimental proof in Figure 9 shows the dependence of T-CARS signal strength on the concentration of alcohol in pure water at C-H stretch band [66,71] ($2900cm^{-1}$). We record the signal intensity at every volume fraction by 20 times to exclude the influence of signal fluctuation. When volume fraction of alcohol gradually increases, concentration dependence transits from strictly linear to sub-quadratic, until quadratic. It is apparent that when volume fraction of alcohol in water is lower than 20%, the

(2900cm$^{-1}$). We record the signal intensity at every volume fraction by 20 times to exclude the influence of signal fluctuation. When volume fraction of alcohol gradually increases, concentration dependence transits from strictly linear to sub-quadratic, until quadratic. It is apparent that when volume fraction of alcohol in water is lower than 20%, the concentration dependence is strictly linear. We prepare the aqueous solution of alcohol with smaller volume fraction intervals to obtain a more precise fitting result. This experiment result consists with the theoretical analysis, and more different samples will be prepared to verify the universality of the theoretical analysis.

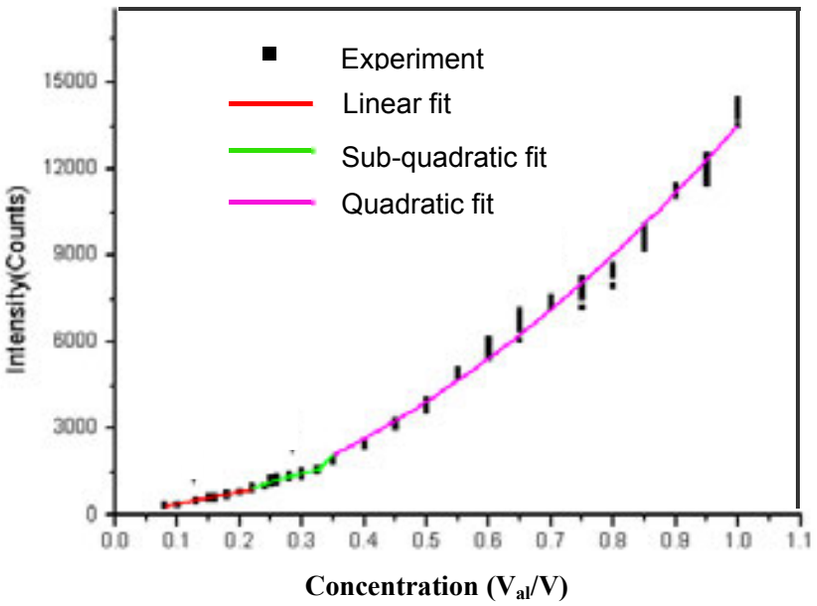


Fig.9 T-CARS intensity for increasing volume fractions of alcohol in water at different volume fraction from 7% to 100%.

### 3.2 Break the lateral diffraction barrier in CARS microscopy

The application of CARS microscopy is limited, nevertheless, by the acquirable lateral spatial resolution, typically around 300nm. With anti-Stokes signal generated from the focal spot, which is then scanned to build up a an image of the sample, a promising way to generate sub-diffraction-limited CARS images is via minimizing the spot to nanometer extent, as in STED[20]. Several schemes have been suggested recently for breaking the diffraction barrier in CARS microscopy, and can be mainly classified as three means: by use of an additional saturation laser to populate coupled vibrational levels, a phase-controlled local oscillator generating ring field at the anti-Stokes frequency being out of phase with the induced CARS field in the focal volume; to add structured illumination for achieving widefield CARS microscopy. Whereas, these schemes still rest on the theory, and no experimental implementations have been reported. And the flows of these schemes are obvious: it's difficult to implement the schemes and can only obtain resolution enhanced images of the molecule specified by the anti-Stokes Raman spectral signal for its particular chemical-bond, not its broadband even total CARS spectral signals; the second method must know the type of the bond in advance, and the third can merely obtain a resolution of around 120nm, etc.

We suggest an approach, the so-called additional probe-beam-induced phonon depletion (APIPD) method[25], to visualize the resolution enhancement by the introduction of an additional

doughnut probe beam with a wavelength that is different from the Gaussian probe beam, which almost synchronizes with the pump and Stokes beams, to deplete the phonons at the periphery of the focal spot. The Gaussian probe beam that immediately follows, with a delay time less than 1ps, will yield anti-Stokes signal in the center but not at the periphery of the focal spot. The difference of the two probe beams in wavelength leads to the disparity of two anti-Stokes signals in spectra, and the signals at the periphery can be filter out by virtue of a particular filter. Consequently, the effective focal spot can be substantially reduced. Super-resolution images can be obtained by scanning the suppressed focal spot.

The rationale of our scheme is to suppress the anti-Stokes signal generation at the periphery of the diffraction-limited spot, i.e., deplete the phonons produced by the pump and Stokes light in this region, then no phonon interact with the probe photons to generate CARS signal here anymore. We adopt an additional probe beam, the first one, with frequency $\omega_{P1}$, which is doughnut-mode, analogy to STED, to achieve this by interacting with phonons to generate useless anti-Stokes signal with frequency $\omega_{A1}$ at the periphery which can be filtered out through a specific filter. The probe beam ($\omega_{P1}$) is nearly simultaneous with the pump and Stokes beams on the sample. The intensity of the first probe beam ($\omega_{P1}$) is strong enough to completely deplete the phonons at the peripheric region, while the immediately followed second probe light ($\omega_{P2}$) with Gaussian profile only generates the useful anti-Stokes signal ($\omega_{A2}$) at the central part of the spot. The time delay between the two probe beams is certainly much smaller than the vibrational dephasing time. The difference of $\omega_{P1}$ and $\omega_{P2}$ results in the disparity of $\omega_{A1}$ and $\omega_{A2}$, therefore we can select the specific filter to filter out the unwanted anti-Stokes signal of frequency $\omega_{A1}$ to obtain the useful signal $\omega_{P2}$ at the suppressed extent of the spot. The process of the APIPD is illustrated as in figure 10.

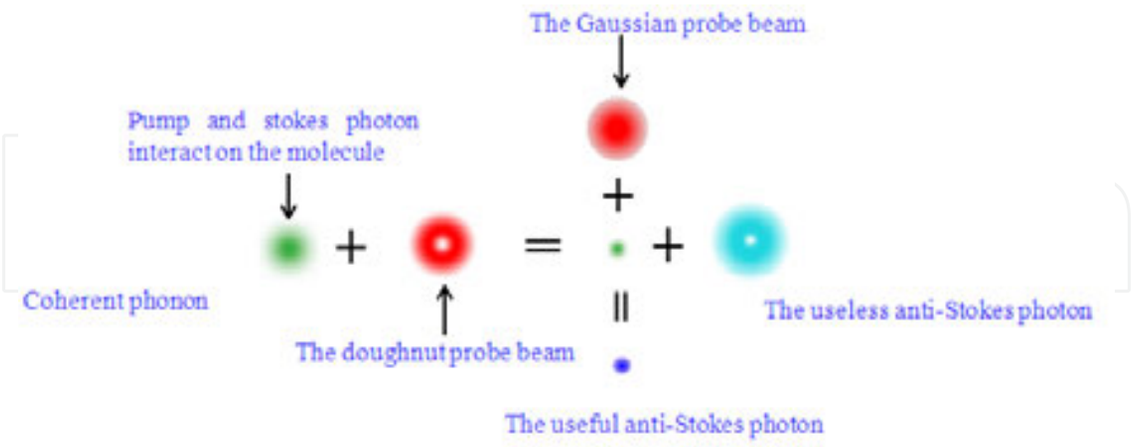


**Figure 10.** The illustration of the process of the APIPD method

$f_S(r)$ and $f_L(r)$ are the Gaussian Stokes and pump beam distribution which can be replaced by squared cosine function, corresponding to that in equation (34). $f_{P1}(r)$ and $f_{P2}(r)$ are the first Gaussian and second doughnut probe beams, respectively, which can be similarly re-

placed by the squared sine and squared cosine functions. Introducing the peak intensities of $I_L^{max}$ , $I_S^{max}$ , $I_{P1}^{max}$ and $I_{P2}^{max}$ representing the pump, Stokes, the first and second probe beams respectively, we have four beams' spatial distribution

$$\begin{aligned} f_L(r) &= I_L^{max}\cos^2(\pi r\mu_L \sin\alpha/\lambda_L) \quad (a) \\ f_S(r) &= I_S^{max}\cos^2(\pi r\mu_S \sin\alpha/\lambda_S) \quad (b) \\ f_{P1}(r) &= I_{P1}^{max} sin^2(\pi r\mu_{P1} sin\,\alpha/\lambda_{P1}) \quad (c) \\ f_{P2}(r) &= I_{P2}^{max} cos^2(\pi r\mu_{P2} sin\,\alpha/\lambda_{P2}) \quad (d) \end{aligned} \tag{34}$$

where $\alpha$ is the semi-aperture of lens and $\mu_L$ , $\mu_S$ , $\mu_{P1}$, $\mu_{P2}$ are the refractive indexes, $\lambda_L$ , $\lambda_S$ , $\lambda_{P1}$ , $\lambda_{P2}$ are the wavelength of the four beams, respectively.

The first doughnut probe light ($\omega_{P1}$) with intensity distribution $f_{P1}(r)$ on the focal plane, almost synchronizes with the pump and Stokes light on the sample. The second Gaussian probe light ($\omega_{P2}$) with intensity distribution $f_{P2}(r)$ follows the first doughnut subsequently within 1 ps much smaller than the vibrational dephasing time. Consequently, after the course of the first probe light, the effective point-spread-function (PSF) of the useful anti-Stokes signal ($\omega_{A2}$) at the suppressed extent of the spot can be expressed as:

$$h^*(r) = f_{P2}(r)\left[n_v - n_v \bullet n_P \bullet \frac{1}{A_{foc}}\partial\sigma_C\right]$$

Hence, the detailed expression of $h(r)$ is

$$h(r) = \begin{cases} h^*(r), & 1 \geq n_P \bullet \frac{1}{A_{foc}}\partial\sigma_C \\ 0, & \text{others} \end{cases} \tag{35}$$

The first term in the square bracket of the equation (35) denotes the total phonon number, and the second term is the phonon number interacting with the first doughnut probe photons at any position of the focal volume. Here A, the cross section area of the volume V, is $V/l$. $N$ is the molecule number. When the second term in the square bracket is not larger than the first term, i.e., phonon number interacting with the first doughnut probe beam is not larger than the total phonon number generated by the pump and Stokes beams, the expression $h^*(r)$ is tenable, or else, the phonons have been depleted before the second probe beam arrives and $h(r)=0$ , therefore, the PSF in the whole space is a piecewise function expressing as:

$$h(r) = \begin{cases} h^*(r) 1 \geq n_P \bullet \frac{1}{A_{foc}}\partial\sigma_C \\ 0 \qquad\qquad\qquad\qquad else \end{cases} \tag{36}$$

http://dx.doi.org/10.5772/59987

The full width at half maximum (FWHM) of $h^*(r)$, denoted by $\Delta r$, is approximated by a Taylor series expansion of $h^*(r)$ to the second order:

$$\Delta r = \sqrt{2}\frac{\lambda}{\pi n \sin\alpha\sqrt{3+K}} \approx \frac{0.9}{\sqrt{3+K}} \bullet \frac{\lambda}{2n\sin\alpha} \tag{37}$$

Here, influence of the refractive index difference and wavelength difference of the pump, Stokes and probe beams are negligible, and both of them are uniformly expressed as $\lambda$ and $n$. $K$ describes magnitude of the doughnut probe beam. Resembling the STED microscopy, the effective PSF, in which the useful anti-Stokes signal ($\omega_{A2}$) is measured, becomes deformed by the unwanted anti-Stokes signal ($\omega_{A1}$) generation. Resolution is enhanced via a factor of square root of the nonlinear order $K$ , namely depletion level, defined by $K = I_{P1}^{max} / I_{P2}^{max}$. Apparently, if no doughnut probe beam introduced, namely $K = 0$, the equation (37) largely reproduces the CARS nonlinear optical microscopy's lateral resolution, which is about $\sqrt{3}$ times better than that of linear optical microscopy. With the gradually increasing of $K$, the lateral spot width decreases continually, following a square-root law, i.e., resolution is increased by a factor of square root of K. In principle, almost no limitation to super-resolution can be obtained. The resolution enhancement technique can yield an effective focal spot which can be fundamentally reduced, theoretically, to an infinitesimal spot, approximating to the size of a molecule or even further to sub-molecular dimensions. Scanning the suppressed spots automatically renders images with resolution breaking the Abbe's diffraction barrier. Our approach can only fundamentally reduce the focal spot in the lateral direction.

Taking $K \approx 50$ to obtain a lateral resolution offor instance, the lateral resolution attainable using this microscopy is approximately ~40 nm, indicating an approach to 5-fold improvement in x or y direction over the diffraction barrier. The PSFs of the traditional and the resolution enhanced CARS microscopy are displayed in figure 11 exploiting the same parameter.

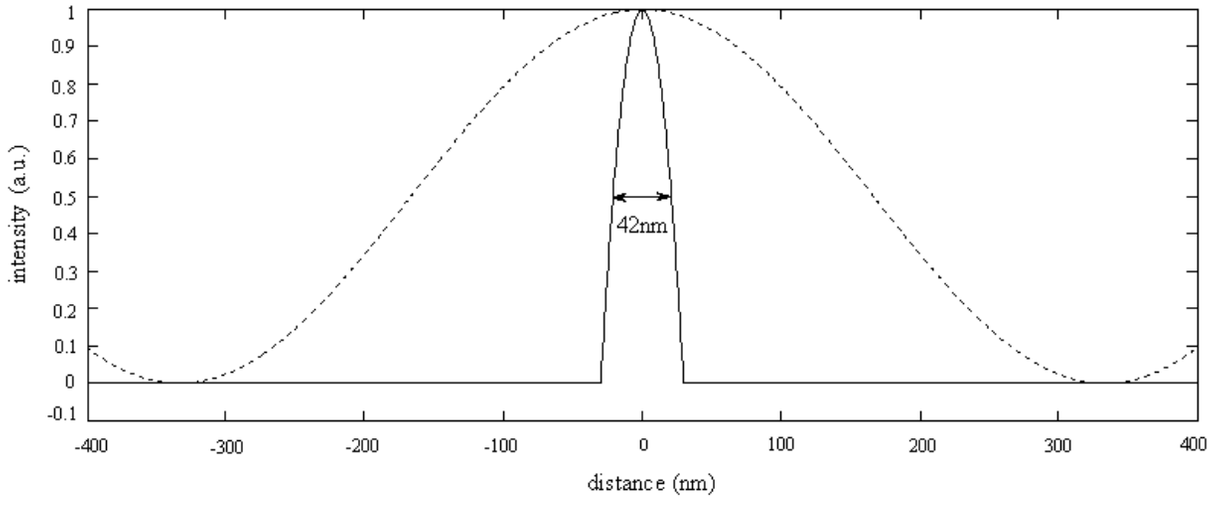


**Figure 11.** Simulation of the point spread function (PSF) of the proposed resolution enhanced CARS microscopy (green, solid line) contrasting with the traditional system (black, dashed line). The new technique indicates that roughly approximate to 8-fold improvement in lateral direction over the diffraction barrier.

In the APIPD scheme, a super-continuum (SC) source generated from a photonic crystal fiber (PCF), as the pump and Stokes pluses, is provided with broad spectral width that allows simultaneous detection over a wide range of Raman shifts. We adopt 500nm and 800nm as the central wavelength of the first and second probe beam, resulting in absolutely distinguishing the two sets of anti-Stokes signals from each other in spectrum. The unwanted anti-Stokes signal on the periphery can be filter out to achieve resolution enhanced images of the molecule specified by its broadband even total CARS spectral signals not only by the anti-Stokes signal of its particular chemical-bond.

### 3.3. SC used in CARS nanoscopy

The traditional CARS device consists of a pump and stokes pulses with a frequency $\omega_L$ and $\omega_S$respectively. And the two beams focus onto a sample after being temporally overlapped. The two waves interact together through the third-order susceptibility to generate a blue-shift anti-stokes signal. CARS being a resonant process, the anti-Stokes signal is strongly enhanced when $\omega_L - \omega_S = \Omega_r$.To avoid the use of two synchronized laser oscillators emitting the pump and Stokes frequencies required in the process, several previous studies have demonstrated multiplex CARS system by using photonic crystal fibers (PCF) [4]. Super-continuum (SC) source generated from a PCF, as the pump and Stokes pluses, is provided with broad spectral width that allows simultaneous detection over a wide range of Raman shifts. The specific and decisive technical advantage in using PCF for CARS measurements is the possibility to generate both pump and Stokes radiations from a single laser. Figure 12 depicts the simple and multiplex CARS process in an energy diagram, the vibrational (or rotational) levels of energy of molecules being schematized by $\omega_R$.

In our scheme, a continuum pulse generated from a PCF, as the pump and Stokes pluses, is provided with broad spectral width that allows simultaneous detection over a wide range of Raman shifts. We adopt 500nm and 800nm as the central wavelength of the first and second probe beam, resulting in absolutely distinguishing the two sets of anti-Stokes signals from each other in spectrum. The unwanted anti-Stokes signal on the periphery can be filter out to achieve resolution enhanced images of the molecule specified by its broadband even total CARS spectral signals not only by the anti-Stokes signal of its particular chemical-bond.

Good compatibility with practical application requirements and acquisition time in CARS microscopy is made with a continuum pulse serving as the Stokes which is generated by injecting ultrashort pulses into a PCF with high nonlinearity. Because of its broad spectra range, frequency difference between the pump and Stokes can cover most of the biologically interesting fingerprint region. Therefore, most distinct vibration modes, perhaps full modes even, can be probed simultaneously by a probe pulse as long as different frequency components in the generated SC propagate at about a same speed, known as broadband CARS spectroscopy.

It is critical to generate a very SC pulse to meet its application in CARS microspectroscopy. To acquire the full CARS spectrum of a certain molecule, the frequency difference should at least cover the fingerprint region from 500 $cm^{-1}$ to 3000 $cm^{-1}$ at a same moment. This determines that the generated SC pulses have the following characteristics: (i) the spectral bandwidth is broad

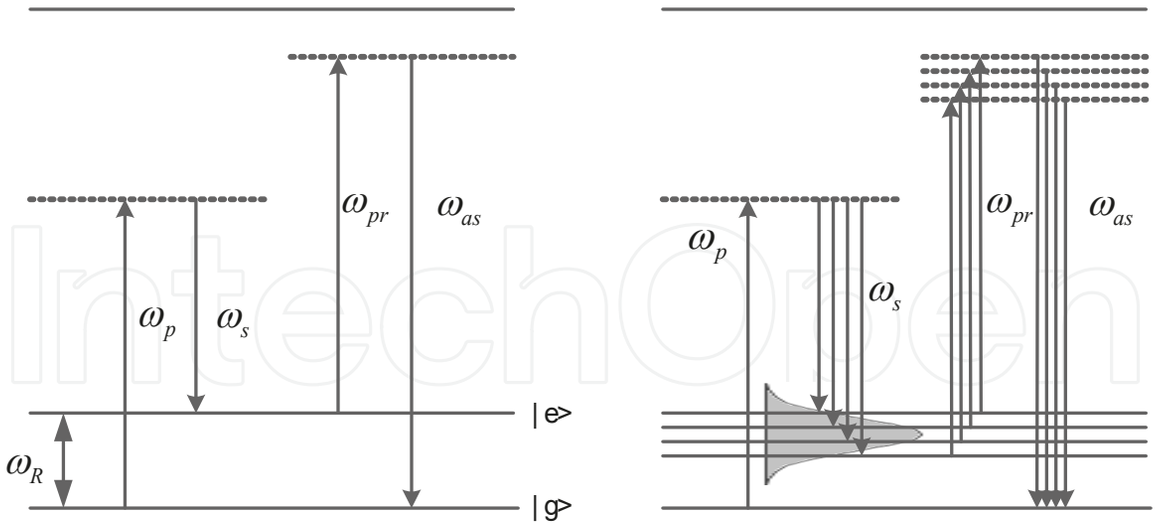


**Figure 12.** Single CARS process (left) and multiples CARS process with a broadband Stokes pulse

enough, (ii) various components in SC propagate at about a same speed, (iii) spectral intensity should be large and uniform.

*3.3.1. SC generation in traditional PCFs*

Although dispersive property of a PCF leads to different propagating velocities of different frequency components in the generated SC, soliton pulse trains from a PCF have been considered as the Stokes in many CARS spectroscopy schemes [75-77]. In this part, we will detailed discuss the generation and characteristics of the soliton pulse trains used in CARS spectroscopy.

When an ultrashort pulse travels in a nonlinear material such as a PCF, different frequency components in it will propagate at different velocity, because of the dispersive effect, including material dispersion and waveguide dispersion. In the anomalous regime, this dispersive effect manifests blue-shift components moving faster than the red-shift components, leading to the temporal broadening. At the same time, SPM generates a nonlinear chirp which is negative near the leading edge and positive near the trailing edge. Therefore the propagating speed decreases near the leading edge and increases near the trailing edge, making the pulse narrow down. Under certain conditions, the optical envelope will keep its shape and propagating velocity known as optical soliton [78,79].

As discussed in section two, distinct peaks in time domain are obvious. Because the soliton ejected earlier has larger group velocity, higher peak power and shorter durations, it will propagate faster than others. So the separation between these peaks becomes larger with a longer propagation distance. Figure 13 shows the spectrograms of the generated SC when the propagation is 10 cm, 15 cm, 20 cm and 25 cm. The input pulse is central at 800 nm with peak power 10kW and pulse duration 50fs as before. From the figures, the first-order soliton shifts from 2 ps to about 8.5 ps when the propagation changes from 10 cm to 25 cm gradually. Also

15 cm, 20 cm and 25 cm. The input pulse is central at 800 nm with peak power 10kW and pulse duration 50fs as before. From the figures, the first-order soliton shifts from 2 ps to about 8.5 ps when the propagation changes from 10 cm to 25 cm gradually. Also the time delay between solitons becomes larger with a longer propagation distance by making contrast of the four graphs. For the dispersion wave on the short wavelength side, time delay between different frequency components also becomes larger. The time span is about 2 ps when the propagation distance is 10 cm, while it is about 5 ps with 25 cm travelling distance. The shifting of solitons in time domain is corresponding to the spectral shifting. The central wavelength of the first-order soliton shifts from 1100 nm to 1200 nm with the propagation from 10 cm to 25 cm.

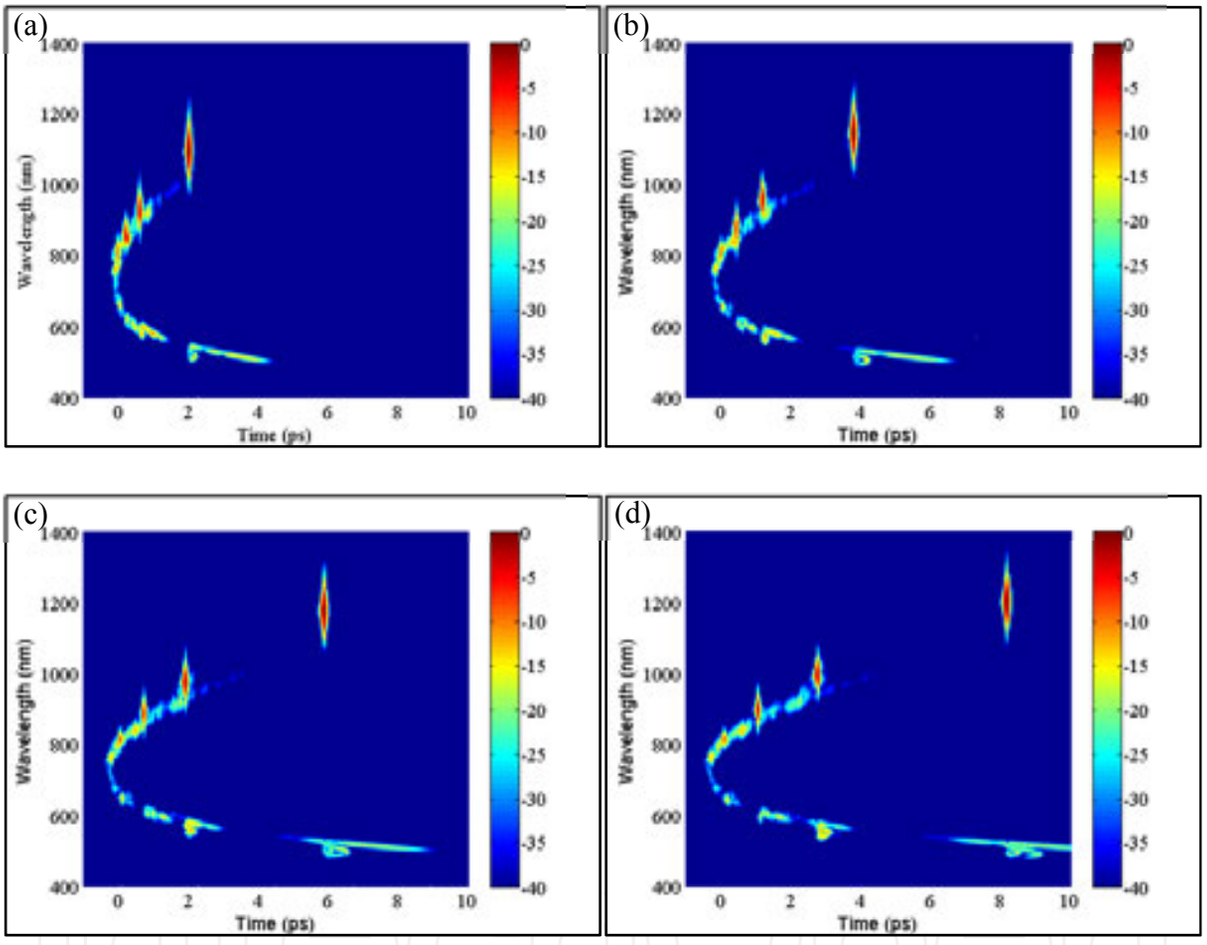


Fig.13 Spectrograms at different propagation distances for input pulse at 800 nm with peak power 10kW and pulse duration 50fs (a) 10 cm; (b) 15 cm; (c) 20 cm; (d) 25 cm;

Although soliton trains will shift towards long-wavelength side due to SSFS [80,81], the pulse duration and spectral bandwidth of first-order soliton are nearly invariable. Figure 14 shows the temporal and spectral profiles of the first-order soliton with different propagating distance with (a) (d) at 10 cm, (b) (e) at 15 cm and (c) (f) at 25 cm. The first-order soliton is selected as both the pump and Stokes just for it has shorter duration and wider spectral bandwidth. It is estimated that the soliton has a pulse duration about 30 fs and spectral bandwidth about 47 nm with 10 cm propagation distance. With further propagation, the pulse duration will increase from 30 to 42 fs, accompanied with the spectral bandwidth decreasing from 47 to 41 nm induced by high-order dispersive and nonlinear effects. Of course the bandwidth is increasing with improving the peak power, but quite few.

http://dx.doi.org/10.5772/59987

nm induced by high-order dispersive and nonlinear effects. Of course the bandwidth is increasing with improving the peak power, but quite few.

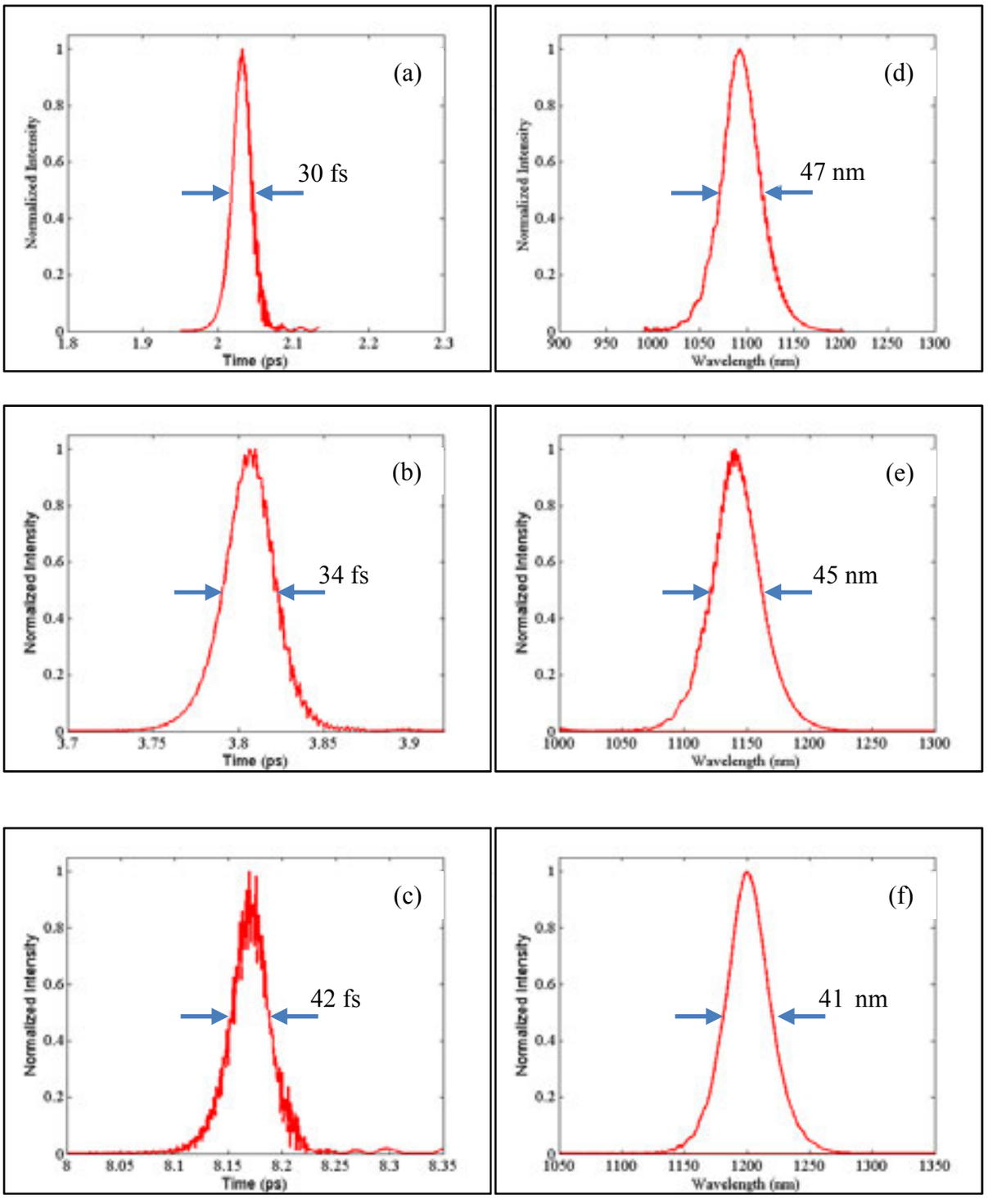


Fig.14 (a ~ c) temporal and (d ~ f) spectral structure of the first-order soliton with (a) (d) at 10 cm, (b) (e) at 15 cm and (c) (f) at 25 cm

**Figure 14.** (a ~ c) temporal and (d ~ f) spectral structure of the first-order soliton with (a) (d) at 10 cm, (b) (e) at 15 cm and (c) (f) at 25 cm

Though this first-order soliton shows good temporal and spectral structures, the limited spectral bandwidth makes it not the best choice for CARS microspectroscopy. That is because the pump and Stokes (soliton pulse) can resonant only few molecular bonds instead of the whole bonds, leading to a CARS spectrum with few Raman distinct peaks. To acquire all the Raman distinct peaks simultaneously, SC with both good temporal structure and broad spectral bandwidth is

Though this first-order soliton shows good temporal and spectral structures, the limited spectral bandwidth makes it not the best choice for CARS microspectroscopy. That is because the pump and Stokes (soliton pulse) can resonant only few molecular bonds instead of the whole bonds, leading to a CARS spectrum with few Raman distinct peaks. To acquire all the Raman distinct peaks simultaneously, SC with both good temporal structure and broad spectral bandwidth is needed.

*3.3.2. SC with all-normal dispersion PCF*

Recent studies show that SC with broad spectral bandwidth, uniform intensity profile and good coherence is obtained by launching ultrashort laser pulses into an all-normal-dispersion PCF [82,83]. These PCFs exhibit a convex dispersive profile which is flat near the maximum dispersion wavelength (MDW). And they possess none ZDW point in the visible and near-infrared spectral region, known as all-normal dispersion. Without anomalous dispersion region, all the soliton related dynamics PCFs supressed, including the SPM effect and optical wave breaking, the SC pulse can keep characteristic of a single pulse during the propagation. And the SC pulse is easy for dispersion compensation with such smooth phase distribution. These properties make the generated SC in all-normal dispersion PCFs especially suit for time-resolved applications, such as CARS spectroscopy.

In the following simulations, an all-normal dispersion PCF (from NKT Photonics) with hole diameter 0.5616 μm and hole pitch 1.44 μm is used. Figure 15 shows the cross-section and dispersion profile of the all-normal dispersion PCF respectively. From figure (b), it is clear that this fiber shows all-normal dispersion in the range from visible to near-infrared. And the dispersion parameter D is estimated about $-10\,\mathrm{ps/nm\cdot km}$ at wavelength about 1060 nm, at which point the nonlinear coefficient is about $37\,\mathrm{W^{-1}m^{-1}}$.

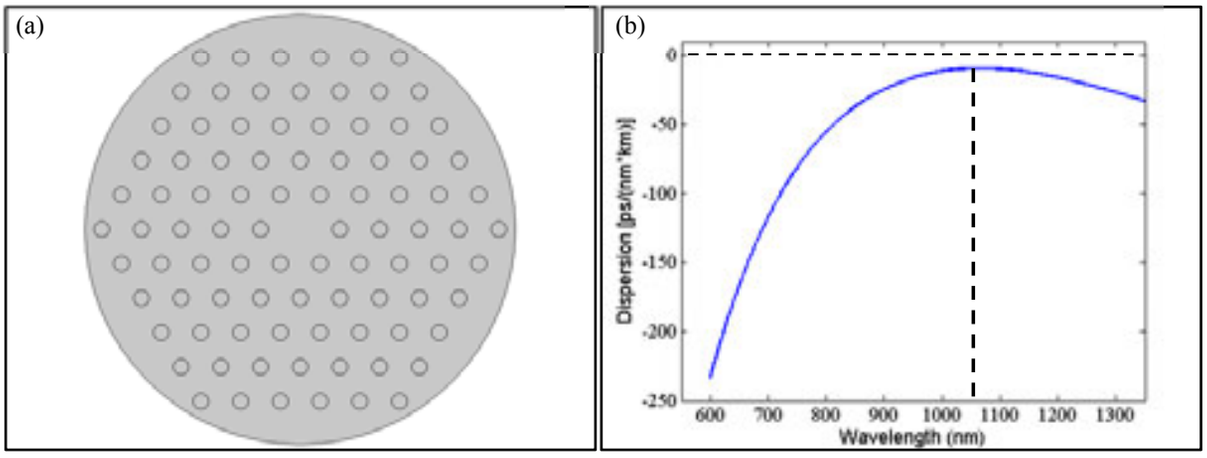


Fig.15 (a) Cross-section model used in simulation and (b) dispersion profile of the all-normal dispersion PCF

**Figure 15.** (a) Cross-section model used in simulation and (b) dispersion profile of the all-normal dispersion PCF

Temporal and spectral evolutions with propagating distance are shown in figure 16 when hyperbolic secant pulses centered at 1060 nm with pulse duration 100 fs and peak power 30 kw are injected into the PCF. From figure 16 (b), the spectral broadening is first concluded at the short wavelength through propagation about 38 mm, then at the long wavelength side about 56mm. The spectrum will gain no more broadening with further propagation, except that the generated SC has a smoother spectral profile. In temporal domain, the pulse duration changes a little in the initial

http://dx.doi.org/10.5772/59987

Temporal and spectral evolutions with propagating distance are shown in figure 16 when hyperbolic secant pulses centered at 1060 nm with pulse duration 100 fs and peak power 30 kw are injected into the PCF. From figure 16 (b), the spectral broadening is first concluded at the short wavelength through propagation about 38 mm, then at the long wavelength side about 56mm. The spectrum will gain no more broadening with further propagation, except that the generated SC has a smoother spectral profile. In temporal domain, the pulse duration changes a little in the initial stage, but increases gradually with further propagation. And the input pulse keeps its character of single pulse all the time in propagation.

To focus more detailed structures in temporal and spectral domain, evolution slices at different propagating distances are plotted in figure 17 with linear scales. The most notable feature in time domain lies in the conservation of a single pulse during the whole propagation. Although the pulse is broadening during the propagation, self-steepening effect leads to a steeper trailing edge which is clear in slices within 3 centimeters' propagation. After that, the pulse edges becomes steeper which makes the pulse shape like a rectangular function, because even weak dispersion effect also brings about significant changes of pulse shape under abundant SPM-induced frequency chirp. Oscillating structure near the trailing edge as shown in the left graph with 3cm propagation derives from pulse distortion induced by high-order dispersion. And the oscillations near pulse edges are related to optical wave breaking [85].

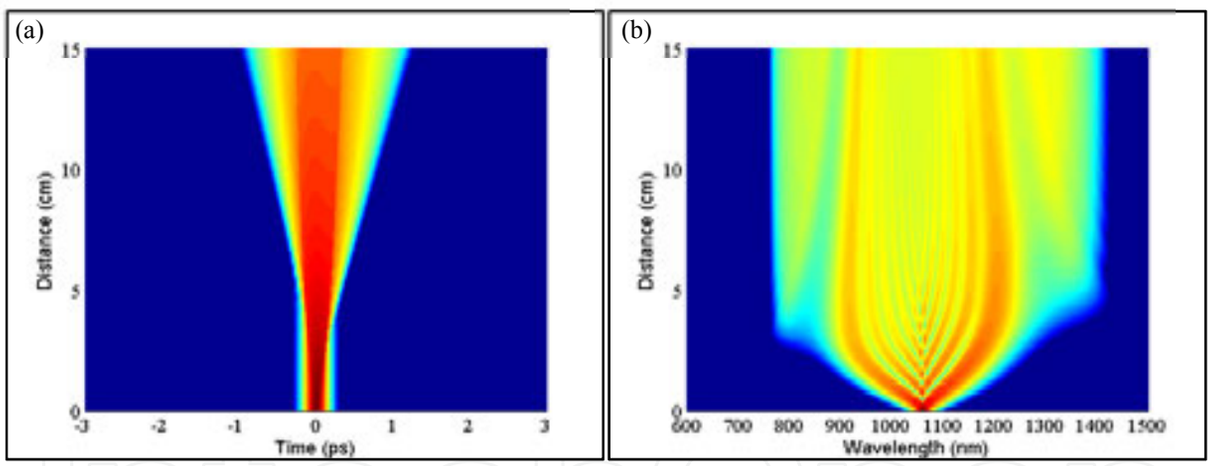


Fig.16 Temporal (left) and spectral (right) evolutions over propagation distance for input pulse centered at 1060 nm with peak power 30 kW and pulse duration 100 fs

**Figure 16.** Temporal (left) and spectral (right) evolutions over propagation distance for input pulse centered at 1060 nm with peak power 30 kW and pulse duration 100 fs

In spectral domain, the spectral broadening induced by SPM effect is significant with a clear oscillating structure through the full wavelength. The SPM-induced spectral broadening spreads out towards two sides of the pump wavelength with red-shift components near the leading edge and blue-shift components near the trailing edge. And in the later propagation, the oscillating structure is explained by optical wave breaking. The red-shift components near the leading edge transfer faster and catch up with the red components near leading edge, leading to the interference between them. The blue-shift components near the trailing edge are just an opposite to that. This oscillating structure in spectral domain and the oscillations near pulse edges in the temporal domain are manifestations of the same phenomenon.

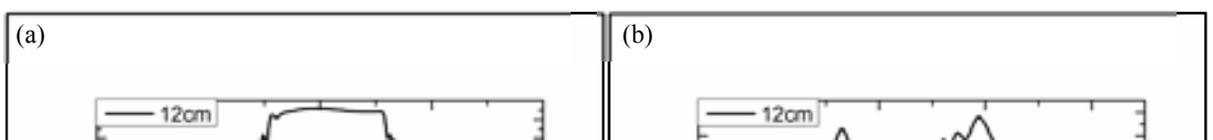

transfer faster and catch up with the red components near leading edge, leading to the interference between them. The blue-shift components near the trailing edge are just an opposite to that. This oscillating structure in spectral domain and the oscillations near pulse edges in the temporal domain are manifestations of the same phenomenon.



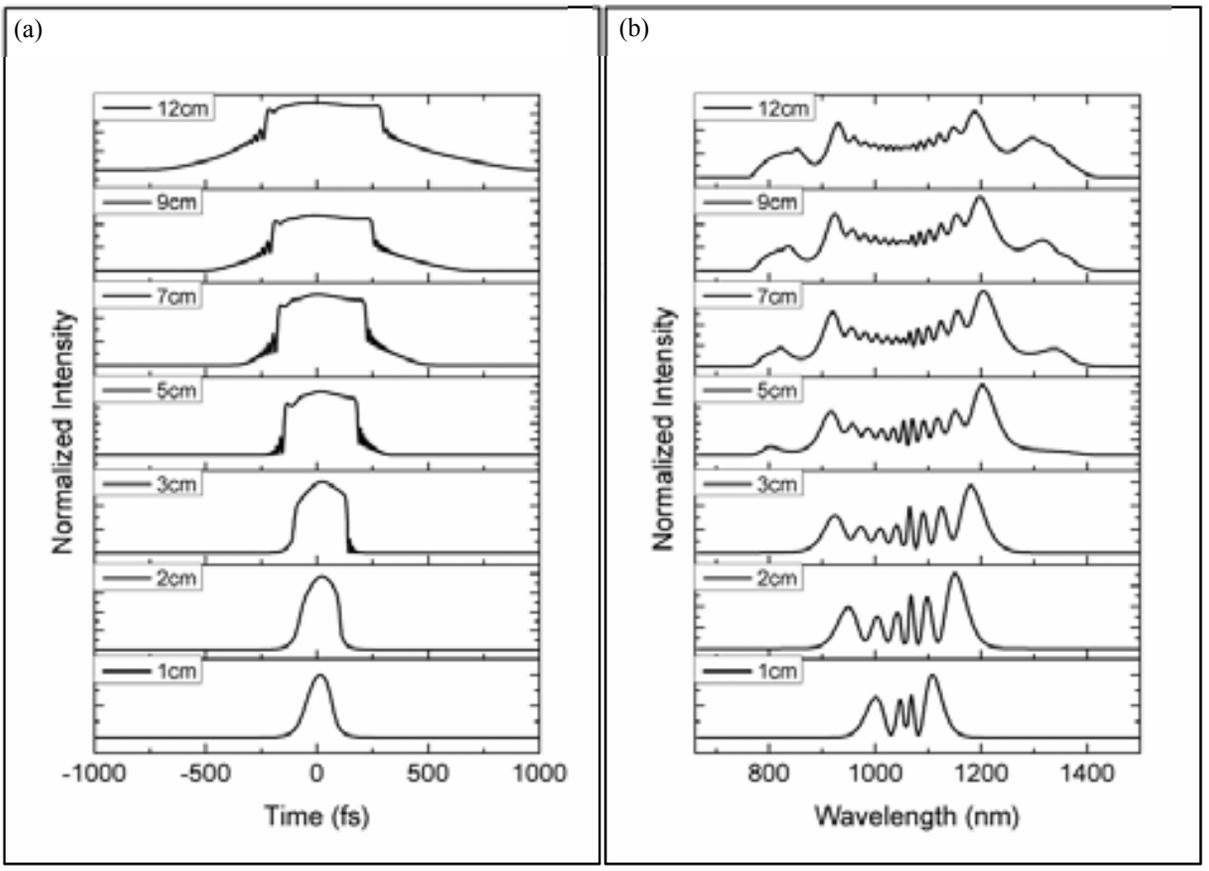


Fig.17 Evolution slices at different propagation distances in temporal (left) and spectral (right) domain

**Figure 17.** Evolution slices at different propagation distances in temporal (left) and spectral (right) domain

Although SC generated in all-normal dispersion PCF has good temporal and spectral structures, it is useful to study the impact of input pulses on the SC generation, such as pulse duration, pulse energy and so on.

First, the central wavelength, pulse duration and fiber length are restricted to show the impact of pulse energy on SC generating. The input pulses are centered at 1060 nm with pulse duration 100 fs and propagation distance 15 cm. Figure 18(a) shows the variations of spectral bandwidth with different pulse energies ranging from 2 nJ to 10 nJ. It is clear that the generated SC shows larger spectral broadening, much more than 600 nm with pulse energy 4 nJ. For a higher pulse energy, the SC generating is much influenced by the SPM and self-steepening effects, leading to the distinct peaks on each side of the pump wavelength. But the intensity near the pump dips more due to them. The spectral bandwidth is increasing, but the increment becomes small, with pulse energy.

Figure 18(b) shows the impact of pulse duration on generated SC with peak power being a constant 30 kW. The relation between peak power and pulse duration is $E=P \bullet \Delta\tau$ with E being pulse energy, P and $\Delta\tau$ being peak power and pulse duration at half maximum. It is clear that the spectral broadening changes few with different pulse durations. The spectrum reaches 600 nm when the peak power keeps 30 kW. With larger pulse duration, the oscillating structures

energy, the SC generating is much influenced by the SPM and self-steepening effects, leading to the distinct peaks on each side of the pump wavelength. But the intensity near the pump dips more due to them. The spectral bandwidth is increasing, but the increment becomes small, with pulse energy.



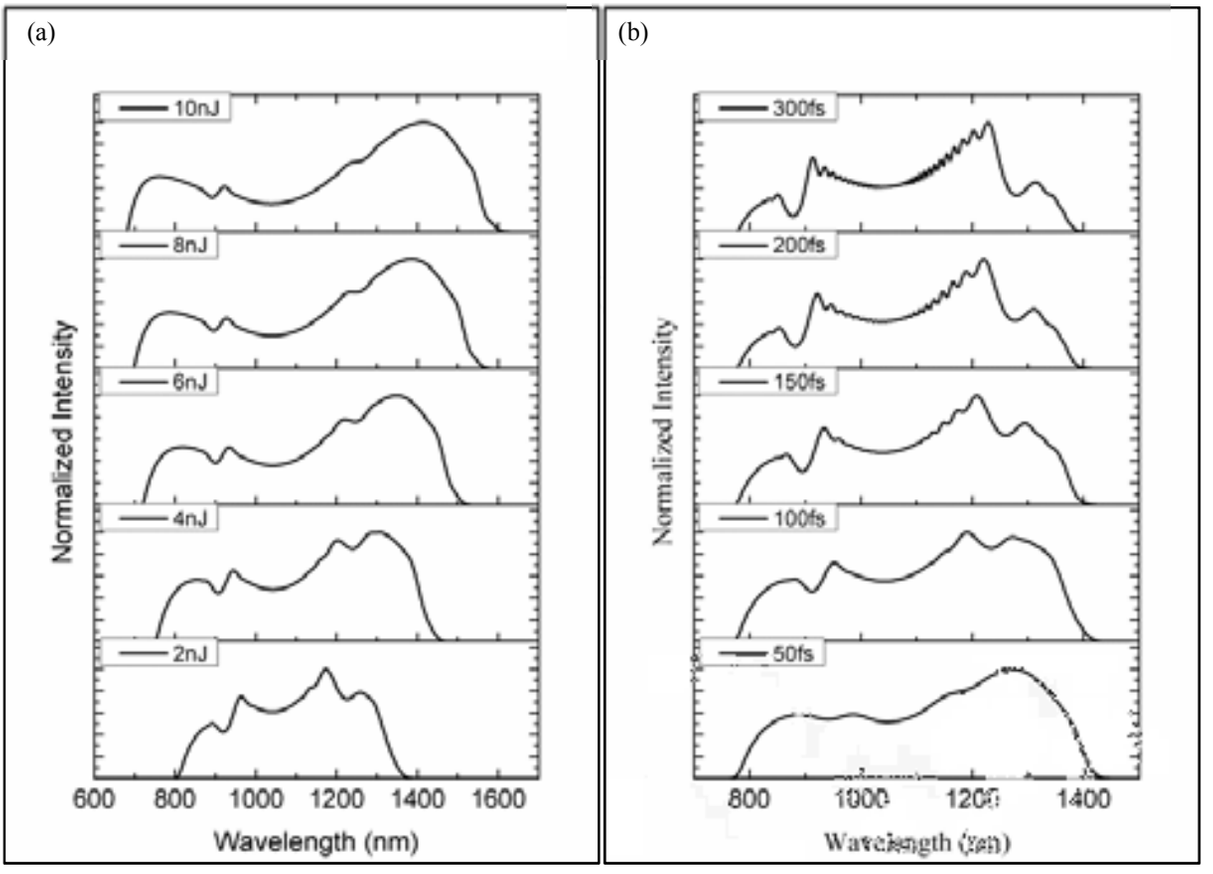


Fig. 18 Spectral broadening with different pulse (a) energies and (b) durations

**Figure 18.** Spectral broadening with different pulse (a) energies and (b) durations

Figure 18(b) shows the impact of pulse duration on generated SC with peak power being a constant 30 kW. The relation between peak power and pulse duration is $E = P \cdot \Delta\tau$ with E being pulse energy, P and $\Delta\tau$ being peak power and pulse duration at half maximum. It is clear that the spectral broadening changes few with different pulse durations. The spectrum reaches 600 nm when the peak power keeps 30 kW. With larger pulse duration, the oscillating structures in output spectrum are more obvious. Also the dips near pump wavelength are much more clear. Due to optical wave breaking induced four-wave mixing, the sidebands at each short and long wavelength side are significant, and their peaks are moving towards short and long wavelength direction respectively.

Although the generated SC has a larger spectral broadening when the PCF is pumped near the MDW, the impacts of central wavelength of input pulses on SC generation are analyzed. In figure 19, temporal and spectral structures of generated SC with different pump wavelengths are plotted where the pulse duration, pulse energy and propagation distance are fixed to 100 fs, 2 nJ and 15 cm respectively. For 1060 nm pump, the spectrum is approximately symmetric from 800 nm to 1350 nm with clear oscillating structures near the pump wavelength. For pump wavelength far from the MDW, not only the full spectrum is shorter that that with 1060 nm pump, but the spectrum shows a tail towards the MDW with much lower amplitude than the peaks induced by SPM. There are obviously small tails near the leading edge for 1200 nm pump and trailing edge for 900 nm pump in figure (a) which are induced by high-order dispersion. These tails will apply additional difficulty to dispersion compensation

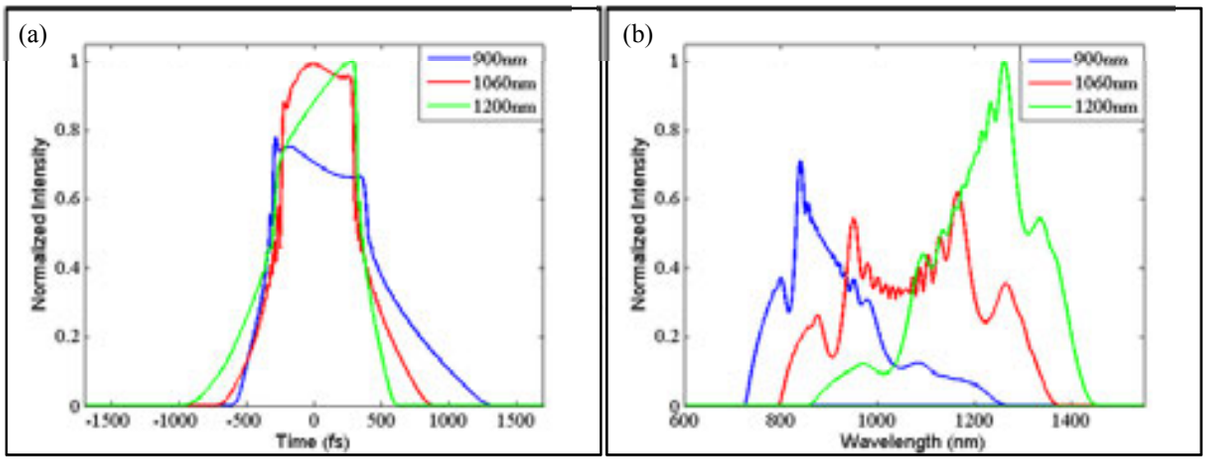


Fig 19 Pulse shapes with different pump wavelengths in (a) temporal and (b) spectral domain

**Figure 19.** Pulse shapes with different pump wavelengths in (a) temporal and (b) spectral domain

From above analyses and discussions, the all-normal dispersion PCF should be pump near the maximum dispersion point with proper peak power and pulse duration to generate an excellent SC suitable for CARS spectroscopy with broad spectral bandwidth, uniform spectral intensities and smooth and excellent temporal structure with smooth phase distribution. The spectral intensity profile is much more smooth with shorter pulse duration under the same peak power. Although higher peak power is beneficial to spectral broadening, it often causes strong tails near the pulse edges and bad flatness of spectral intensity profile. And the fiber length is also very important, because a longer fiber length makes a more flat spectral profile while temporal structure becomes bad.

Based on the basic experimental facilities, pulses centered at 1060 nm with pulse duration 50 fs and pulse energy 2nJ are injected into the all-normal dispersion PCF. The spectrum of output pulse can be expanded to 600~ nm (from ~800 nm to 1400~ nm) after 12 cm propagation with the spectrogram of generated SC being displayed in figure 20(a). This SC shows good spectral continuity and uniformity with tails on both the long and short wavelength sides caused by high-order dispersion. Figure 20(b) demonstrates the temporal distribution of the generated SC pulse with slightly asymmetric structure towards the tailing edge. And the tails on long and short wavelength sides are related to the pedestals near leading and trailing edges. From figure (b), the delay time between different components is less than 2 ps and the temporal phase is predominantly quadratic, which makes the dispersion compensation much easier.

To exploit this continuum pulse into CARS spectroscopy, it is necessary to compensate the delay time induced by dispersive effect and other nonlinear effects, leading to a same propagating speed of different frequency components. In terms of such small dispersion, a pair of prisms made of BK7 glass are used to compensate it. The spectrogram and temporal, spectral profiles after dispersion compensation are plotted in figure 21, with (a) being the spectrogram, (b) the temporal profile and (c) the spectral profile. After dispersion compensation, most components in the generated SC are propagating at a same speed, except the tails on long and short wavelength sides, for the prisms are not effective enough to compensation of high-order dispersion. From figure (b), the pulse duration of generated SC is compressed to about 15 fs from initial ~2 ps in spite of a little oscillation near the pulse edges. Figure (c) shows the spectral profile on a linear scale with bandwidth over 600 nm. And the spectral intensity possesses a good uniformity.

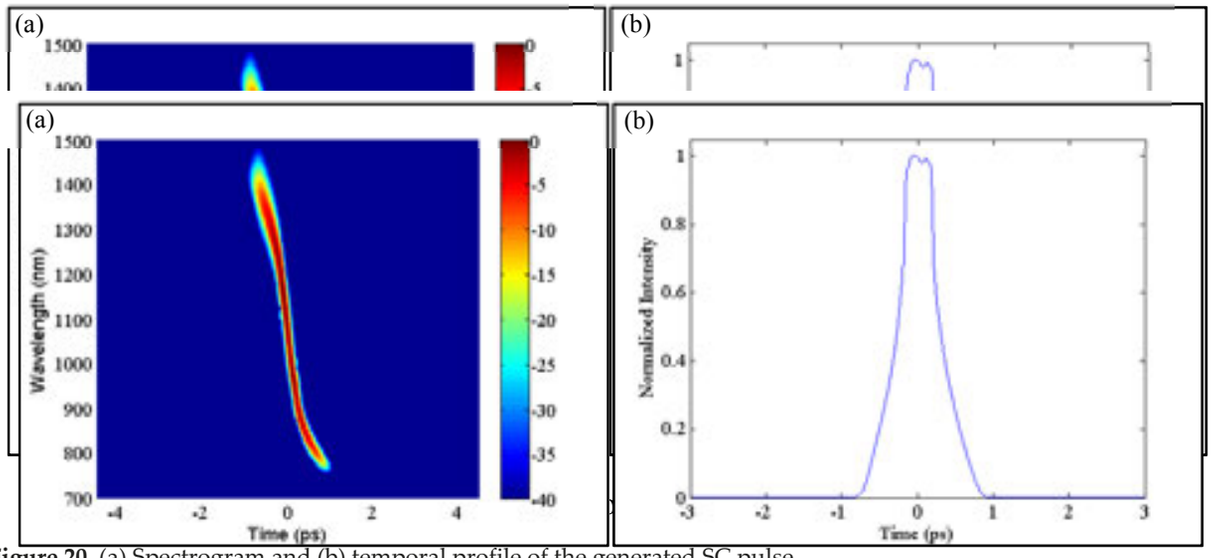


**Figure 20.** (a) Spectrogram and (b) temporal profile of the generated SC pulse

Fig.20 (a) Spectrogram and (b) temporal profile of the generated SC pulse

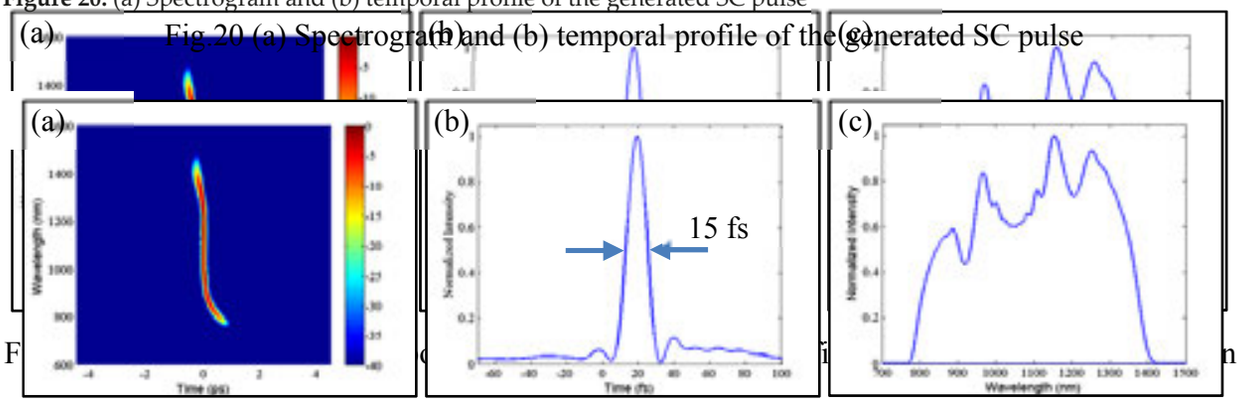


Fig.21 (a) Spectrogram, (b) temporal profile and (c) spectral profile after dispersion compensation

**Figure 21.** (a) Spectrogram, (b) temporal profile and (c) spectral profile after dispersion compensation

Supposing that the delay time between different frequency components is limited to less than 40 fs, it is estimated that the useful components still span over 400 nm from 900 to 1300 nm. This SC after dispersion compensating shows wonderful temporal structures, broad spectral bandwidth, and uniform spectral intensity, which make it well suited for time-resolved applications, especially CARS microspectroscopy. To make the best of the tails in figure (a), spatial light modulator is suggested for the high-order dispersion compensation[86,87].

Supposing that the delay time between different frequency components is limited to less than 40 fs, it is estimated that the useful components still span over 400 nm from 900 to 1300 nm. This SC after dispersion compensating shows wonderful temporal structures, broad spectral bandwidth, and uniform spectral intensity, which make it well suited for time-resolved applications, especially CARS microspectroscopy. To make the best of the tails in figure (a), spatial light modulator is suggested for the high-order dispersion compensation[86,87].

# 4 Supercontinuum used in infrared nanoscopy

4. Supercontinuum used in infrared nanoscopy

## 4.1 Theory of infrared absorption spectroscopy

4.1. Theory of infrared absorption spectroscopy

The infrared (IR) absorption spectroscopy is an excellent method for biological analyses. It enables the nondestructive, label-free extraction of biochemical information and images[27,88]. The physical basis of IR absorption is that, when an infrared light interacts with the molecule, the vibrations or rotations in a molecule may cause a net change in the dipole moment. The alternating electrical field of the radiation interacts with fluctuations in the dipole moment of the molecule. If the frequency of the radiation matches the vibrational frequency of the molecule, then the radiation will be absorbed[89,90]. Every material has its unique IR absorption spectra that can be used as a "fingerprint" for identification. Absorption in the infrared region results in changes in vibrational and rotational status of the molecules. The absorption frequency depends on the

The infrared (IR) absorption spectroscopy is an excellent method for biological analyses. It enables the nondestructive, label-free extraction of biochemical information and images[27,88]. The physical basis of IR absorption is that, when an infrared light interacts with the molecule, the vibrations or rotations in a molecule may cause a net change in the dipole moment. The alternating electrical field of the radiation interacts with fluctuations in the dipole moment of the molecule. If the frequency of the radiation matches the vibrational frequency of the molecule, then the radiation will be absorbed[89,90]. Every material has its unique IR absorption spectra that can be used as a "fingerprint" for identification. Absorption in the infrared region results in changes in vibrational and rotational status of the molecules. The absorption frequency depends on the

moment of the molecule. If the frequency of the radiation matches the vibrational frequency of the molecule, then the radiation will be absorbed [89,90]. Every material has its unique IR absorption spectra that can be used as a "fingerprint" for identification. Absorption in the infrared region results in changes in vibrational and rotational status of the molecules. The absorption frequency depends on the vibrational frequency of the molecule, whereas the absorption intensity depends on how effectively the infrared photon energy can be transferred to the molecule, and on the change in the dipole moment that occurs as a result of molecular vibration [91-93]. In a word, a molecule will absorb infrared light only if the absorption causes a change in the dipole moment. Infrared spectroscopy is widely applied to various samples such as liquid, gas, and solid-state matter to identify and to quantify the unknown materials. It is an effective technique to identify compounds and is used extensively to detect functional groups.

Collecting of IR spectra signal usually occurs in two different ways. One is the conventional dispersive-type spectrometer, which employs a grating or a prism to disperse light into individual frequencies, and a slit placed in front of the detector to determine which frequency to reach the detector [94]. However, dispersive-type spectrometer is outdated today. Modern IR spectrometers are the so-called Fourier transform infrared absorption (FTIR) spectroscopy instruments [95,96]. All the FTIR spectrometer operates on the Fourier transform principle, and refers to the manner in which the data is collected and converted from an interference pattern to a spectrum. FTIR spectrometers have progressively replaced the dispersive instruments for most applications due to their superior speed and sensitivity. They have greatly extended the capabilities of IR spectroscopy and have been applied to many fields that are very difficult or nearly impossible to study by dispersive instruments [97,98]. FTIR can be utilized to measure some components of an unknown mixture and is currently applied to the analysis of solids, liquids, and gases.

The Basic FTIR System as shown in figure 22, there are mainly four parts: Light source, interferometer, sample compartment, and the detector. The beam splitter divides the incoming infrared beam into two beams. One beam reflects off the fixed mirror, and the other beam reflects off the moving mirror, constituting a Michelson interferometer. After reflected from the two mirrors, the divided beams meet each other again at the beam splitter. Approximately 50% of the light passes through the beam splitter and is reflected back along its path by a fixed mirror, and half of the light is reflected by the same beam splitter. The other 50% fraction of the incident light is reflected onto a moving mirror. Light from the moving mirror returns along its original path and half of the light intensity is transmitted through the beam splitter. The two beams meet again at the same beam splitter and then pass through the sample cell, to the infrared sensor. Thus 25% of the incident light from the source reaches the sensor from the fixed mirror and 25% from the moving mirror. As the path length of the two light beams striking the sensor will differ, there will be destructive and constructive interference.

The beam from the moving mirror has traveled a different distance than the beam from the fixed mirror. When the two beams are combined by the beam splitter, an interference pattern is created, since some of the wavelengths recombine constructively and some destructively. This interference pattern is called an interferogram. This interferogram then goes from the

http://dx.doi.org/10.5772/59987

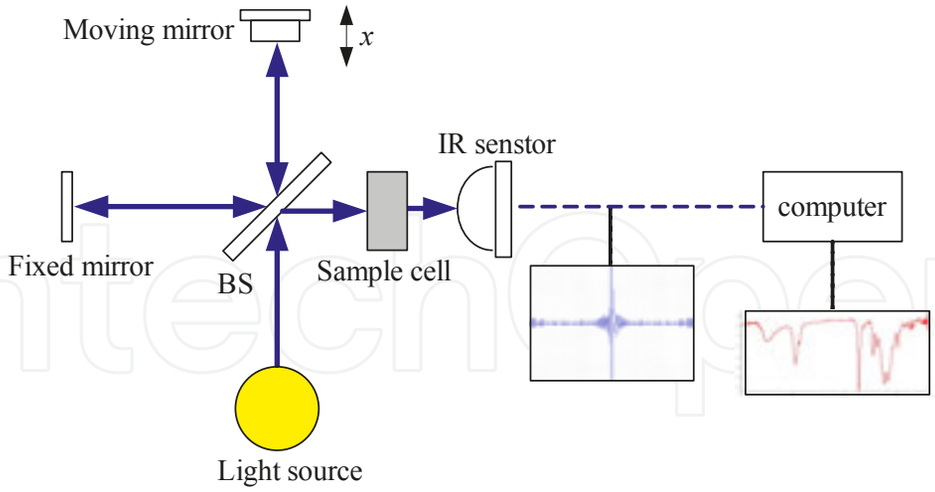


**Figure 22.** The main components of a FTIR

beam splitter to the sample, where some energy is absorbed and some is transmitted. The transmitted portion reaches the detector. Every stroke of the moving mirror in the interferometer equals one scan of the entire IR source spectrum, and individual scan can be combined to give better representation of the actual absorbance of the sample. Each point in the interferogram contains information from each wavelength of light being measured. The detector reads information about every wavelength in range of the IR source simultaneously. To obtain the infrared spectrum, the detector signal is sent to the computer, and an algorithm called a Fourier transform is performed on the interferogram to convert it into a spectrum. This transmittance spectrum can be converted to absorbance. The process of collecting the IR spectrum in an FTIR spectrometer is illustrated in figure 23. FTIR spectrometer simultaneously collects spectral data in a wide spectral range of the IR source [99]. In contract, in a dispersive spectrometer, every wavelength across the spectrum must be measured individually. This is a slow process, and typically only one measurement scan of the sample is made. Accordingly, the superior speed and sensitivity of FTIR is the significant advantage over a conventional dispersive spectrometer which measures intensity over a narrow range of wavelengths at a time [100,101].

The FTIR refers to the manner in which the data is collected and converted from an interference pattern to a spectrum. The FTIR spectrometer operates on a principle called Fourier transform. The mathematical expression of Fourier transform can be expressed as

$$F(\omega)=\int_{-\infty}^{+\infty} f(x)e^{i\omega x}dx \tag{38}$$

And the reverse Fourier transform is

$$f(x)=\frac{1}{2\pi}\int_{-\infty}^{+\infty} f(x)e^{-i\omega x}d\omega \tag{39}$$

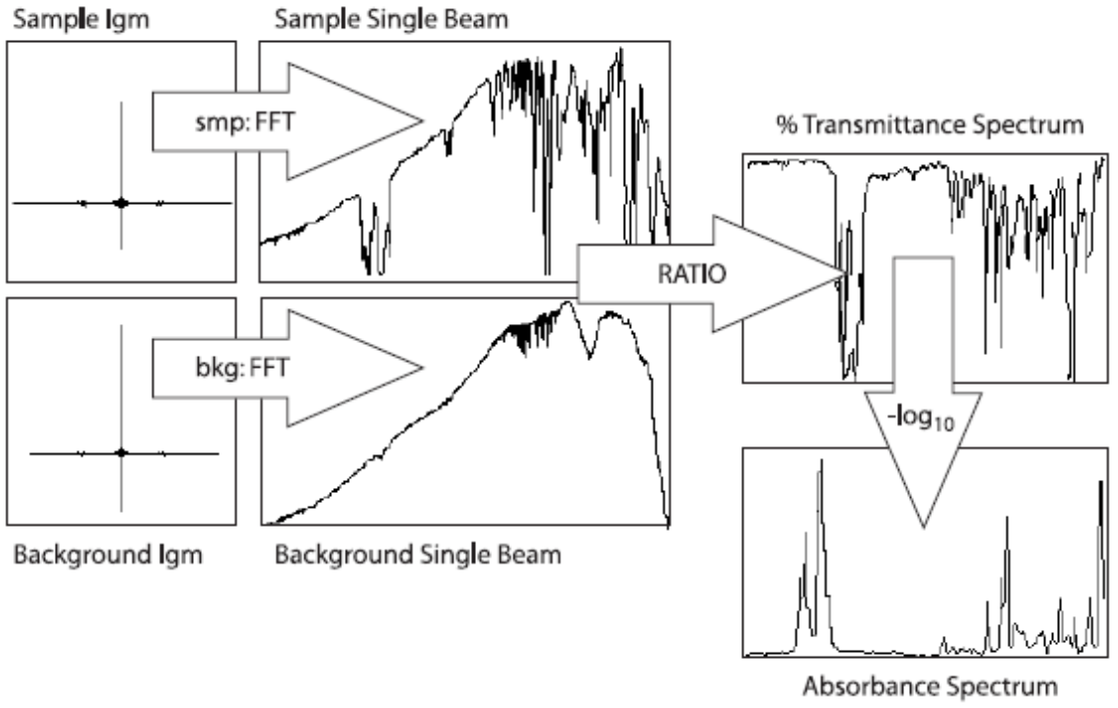


**Figure 23.** The process of collecting the IR spectrum in an FTIR spectrometer

where $\omega$ is angular frequency and $x$ is the optical path difference. $F(\omega)$ is the spectrum and $f(x)$ is called the interferogram. It is clear that if the interferogram $f(x)$, is determined experimentally by using the Michelson interferometer, the spectrum F($\omega$) can be obtained by using Fourier transform. The detector receives a signal, i.e., the interferogram, which is a summation of all the interferences resulting from the constructive and destructive interaction between each wavelength component and all the others. The two most popular detectors for a FTIR spectrometer are deuterated triglycine sulfate (pyroelectric detector) and mercury cadmium telluride (photon or quantum detector). The measured signal is sent to the computer where the Fourier transformation takes place.

FTIR spectrometer simultaneously collects spectral data of the IR in a wide spectral range. This confers a significant advantage over a dispersive spectrometer which measures intensity over a narrow range of wavelengths at a time. FTIR spectrometers have progressively replaced dispersive instruments for most applications due to their superior speed and sensitivity, and opens up new applications of infrared spectroscopy

### 4.2. SC used in IR nanoscopy

FTIR spectroscopy is a widely used analytical tool for chemical identification of inorganic, organic, and biomedical materials, as well as for exploring conduction phenomena [102-104]. Because of the diffraction limit, however, conventional FTIR cannot achieve nano-scaled resolution [105]. Therefore a FTIR system that allows for infrared-spectroscopic nano-imaging is required. The ability to use a spectrally broad source in a FTIR system makes this technique

http://dx.doi.org/10.5772/59987

promising at the nano-scale for the chemical identification of unknown nanostructures. Relying on the use of scattering-type scanning near-field optical microscopy [106,107] (s-SNOM), the diffraction limit of a FTIR system is overcome by the use of a sharp atomic force microscope (AFM) tip acting as an antenna to concentrate the incident radiation to nano-scaled volumes [108-110]. Recording of the tip-scattered light thus yields nano-scaled resolved optical images. With the introduction of s-SNOM, the diffraction-limited resolution in FTIR microscopy can be overcome by several orders of magnitude. Nano-FTIR has interesting application potential in widely different sciences and technologies.

Traditional FTIR spectrometers are based on either thermal IR sources with low brightness and coherence, such as a globar or Hg-lamp, or synchrotron radiation. The synchrotron radiation is complex, expensive, power consuming and always accompanied with intensity fluctuation in spite of high brightness and coherence [29,111]. The advent of non-silica fibers brings us a new IR source with both high brightness and coherence, not to mention the broad bandwidth [31,33,112,113]. Besides fused silica, the PCFs can also be made of other materials, such as chalcogenide and fluoride which show novel characteristics near mid-infrared, such as high transmissivity. Based on these materials, the PCF can shift its ZDW to mid-infrared region, which makes the SC generation in mid-infrared realized easily [114]. And their intrinsic high IR transmissivity and nonlinear coefficient makes it especially suit for mid-infrared SC generation. With these materials, step-index fibers, tapered fibers and photonic crystal fiber can be used to generate the mid-infrared SC [115,116]. Under properly pumping condition, the generated SC shows an ultra-broad spectrum range from 2 μm to 12 μm. These mid-infrared supercontinuum possess a broad spectral bandwidth, higher brightness and coherence [117]. The nano-FTIR combing with such a mid-infrared supercontinuum source, has interesting application potential in widely different sciences and technologies, ranging from the semiconductor industry to nanogeochemistry.

In the following paragraphs, we will discuss the process of SC generation with the widely used PCF made of chalcogenide glass. It is necessary to figure out the refraction index and nonlinear response, because they often vary a lot for different materials. The refraction index of bulk $As_2Se_3$ glass is approximate to the Sellmeier equation as in Eq. (21). The approximate profile show good agreement with measured data [118].

$$n^2(\lambda)=1+\lambda^2\left[\frac{A_0^2}{\lambda^2-A_1^2}+\frac{A_2^2}{\lambda^2-19^2}+\frac{A_4^2}{\lambda^2-4A_1^2}\right] \tag{40}$$

with n($\lambda$) being the refraction index, $\lambda$ the input wavelength expressed in microns. The related Sellmeier coefficients are $A_0$=2.234921, $A_1$=0.24164, $A_2$=0.347441, $A_4$=1.308575. By calculation, the variations of refractive index and dispersion parameter with wavelength are shown in figure 24(a) with $n$ being the refractive index, $n_g$ the group index. It is clear the group index $n_g$ decreases with wavelength below about 7.2 μm and increases beyond that wavelength point. Figure 24(b) exhibits the variation of dispersion with wavelength, where single ZDW point locates in the region from 2 to 14 μm.

point. Figure 24(b) exhibits the variation of dispersion with wavelength, where single ZDW point locates in the region from 2 to 14μm .

point. Figure 24(b) exhibits the variation of dispersion with wavelength, where single ZDW point locates in the region from 2 to 14μm .

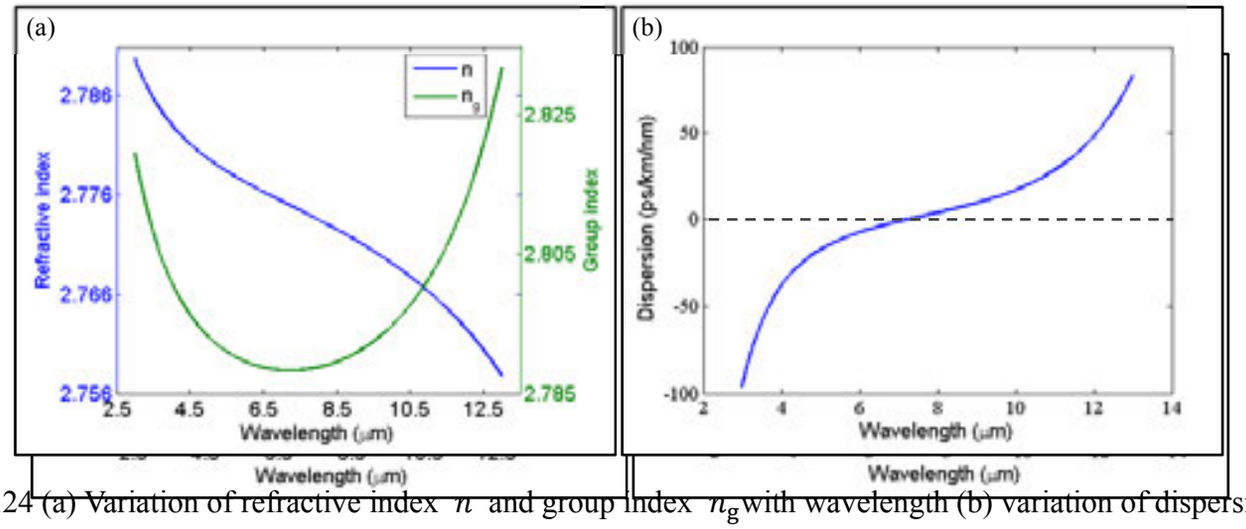


Fig.24 (a) Variation of refractive index $n$ and group index $n_g$ with wavelength (b) variation of dispersion parameter with wavelength

Fig.24 (a) Variation of refractive index $n$ and group index $n_g$ with wavelength (b) variation of dispersion parameter with wavelength

**Figure 24.** (a) Variation of refractive index $n$ and group index $n_g$ with wavelength (b) variation of dispersion parameter with wavelength

Considering the $As_2Se_3$-based PCF has an air hole diameter about 1.2 μm and a hole pitch about 3.0 μm. The ideal structure used in FEM is plotted as in figure 25(a) with a solid core surrounded by four hexagonal rings of air holes. And figure 25(b) shows the dispersion profile of this PCF with single ZDW about 3.72μm. To obtain a larger spectral broadening, this PCF is pump in the anomalous dispersion regime near ZDW, saying 3.75μm, at which the nonlinear coefficient is about $2.7\mathrm{m}^{-1}\mathrm{W}^{-1}$. The nonlinear coefficient in $As_2Se_3$-based PCF is tens to hundreds times larger than that in fused silica due to the higher nonlinear refractive index$n_2$ about $2.4\times10^{-17}\mathrm{m}^2/\mathrm{W}$.

Considering the $As_2Se_3$-based PCF has an air hole diameter about 1.2 μm and a hole pitch about 3.0 μm. The ideal structure used in FEM is plotted as in figure 25(a) with a solid core surrounded by four hexagonal rings of air holes. And figure 25(b) shows the dispersion profile of this PCF with single ZDW about 3.72μm. To obtain a larger spectral broadening, this PCF is pump in the anomalous dispersion regime near ZDW, saying 3.75μm, at which the nonlinear coefficient is about $2.7\mathrm{m}^{-1}\mathrm{W}^{-1}$. The nonlinear coefficient in $As_2Se_3$-based PCF is tens to hundreds times larger than that in fused silica due to the higher nonlinear refractive index$n_2$ about $2.4\times10^{-17}\mathrm{m}^2/\mathrm{W}$.

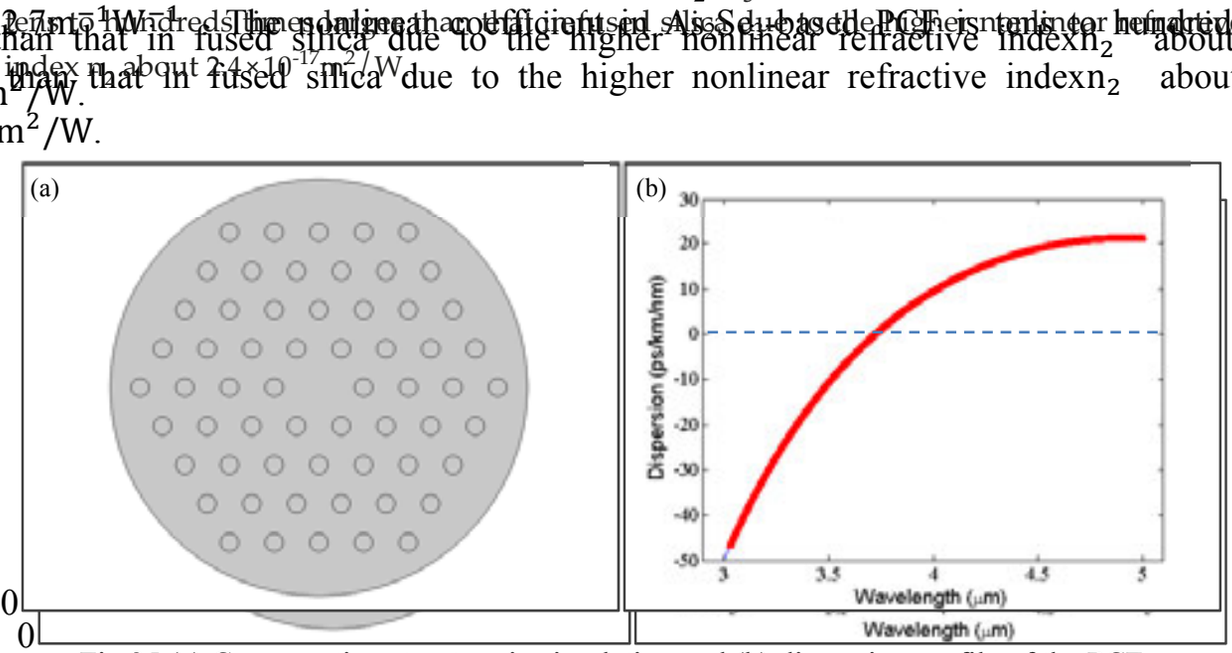


Fig.25 (a) Cross-section structure in simulation and (b) dispersion profile of the PCF

Fig.25 (a) Cross-section structure in simulation and (b) dispersion profile of the PCF

**Figure 25.** (a) Cross-section structure in simulation and (b) dispersion profile of the PCF

Before modeling the process of SC generation in this $As_2Se_3$-based PCF, it is necessary to figure out the nonlinear response function$R(t) = (1-f_R)\delta(t) + f_R h_R(t)$, due to the different materials. For chalcogenide glasses, the fractional contribution of the Raman response to the total nonlinear response is $f_R = 0.115$ and the delayed Raman response function$h_R(t)$ can be expressed as[118,119]

Before modeling the process of SC generation in this $As_2Se_3$-based PCF, it is necessary to figure out the nonlinear response function$R(t) = (1-f_R)\delta(t) + f_R h_R(t)$, due to the different materials. For chalcogenide glasses, the fractional contribution of the Raman response to the total nonlinear response is $f_R = 0.115$ and the delayed Raman response function$h_R(t)$ can be expressed as[118,119]

$$h_R(t) = \frac{\tau_1^2+\tau_2^2}{\tau_1\tau_2^2}\exp\left(-\frac{t}{\tau_2}\right)\sin\left(\frac{t}{\tau_1}\right) \quad (41)$$

$$h_R(t) = \frac{\tau_1^2+\tau_2^2}{\tau_1\tau_2^2}\exp\left(-\frac{t}{\tau_2}\right)\sin\left(\frac{t}{\tau_1}\right) \quad (41)$$

http://dx.doi.org/10.5772/59987

nonlinear response is $f_R$=0.115 and the delayed Raman response function $h_R(t)$ can be expressed as [118,119]

$$h_R(t) = \frac{\tau_1^2 + \tau_2^2}{\tau_1 \tau_1^2} \exp\left(-\frac{t}{\tau_2}\right) sin\left(\frac{t}{\tau_1}\right) \tag{41}$$

with $\tau_1$=23.1 fs, $\tau_2$=195 fs.

In the simulation, the injected pulse has a hyperbolic secant profile with with 200 fs pulse duration and 30 W peak power. The temporal and spectral evolutions of input pulse with propagating distance are plotted in figure 26. It is clear that the output spectral bandwidth reaches 1.6μm from 3 μm to about 4.7μm after propagating about 20 cm. Further propagation brings in only little spectral broadening on the long-wavelength side, which is induced by intrapulse Raman scattering. In time domain, strongly temporal compression occurs within about 11 cm. After that, there is an obvious pulse broadening and soliton fission. Because different frequency components often possess different velocities, time delay between different frequencies becomes larger with a longer propagation,.

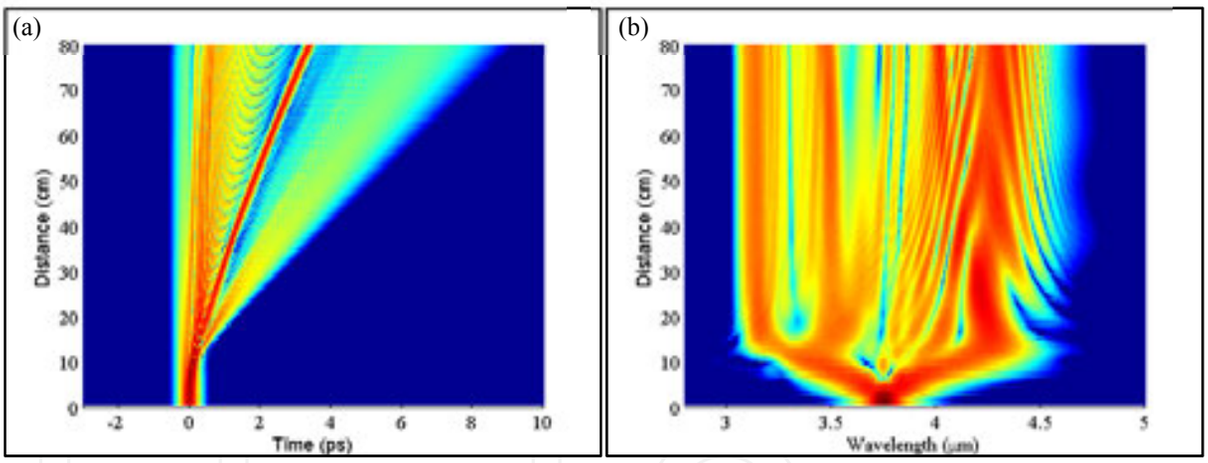


Fig.26 Temporal (a) and spectral (b) evolutions over propagation distance for input pulse centered at 3.75 μm with peak power 30 W and pulse duration 200 fs

**Figure 26.** Temporal (a) and spectral (b) evolutions over propagation distance for input pulse centered at 3.75 μm with peak power 30 W and pulse duration 200 fs

To elaborate on the dynamics of SC generation, different spectral slices are exhibited in figure 27(a) on a logarithmic scale. All the spectrums in figure 27(a) are cut off at -80 dB. In the initial propagation stage, spectral broadening is approximately symmetrical. And the main mechanism of spectral broadening is SPM effect. The SPM-induced spectral broadening has a notable oscillation structure with the outermost peaks possessing the most intense as shown in figure. After around 12 cm, the spectral broadening becomes asymmetric with a larger broadening on the long wavelength side. The out side peaks on long- and short-wavelength side are related to soliton fission and dispersive wave generation. With further propagation, spectrum on long-wavelength side spans little due to weak Raman scattering.

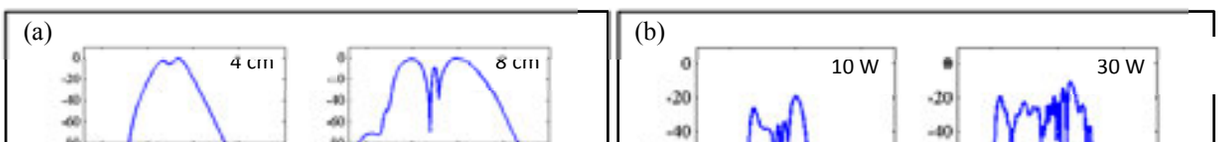

notable oscillation structure with the outermost peaks possessing the most intense as shown in figure. After around 12 cm, the spectral broadening becomes asymmetric with a larger broadening on the long wavelength side. The out side peaks on long- and short-wavelength side are related to soliton fission and dispersive wave generation. With further propagation, spectrum on long-wavelength side spans little due to weak Raman scattering.

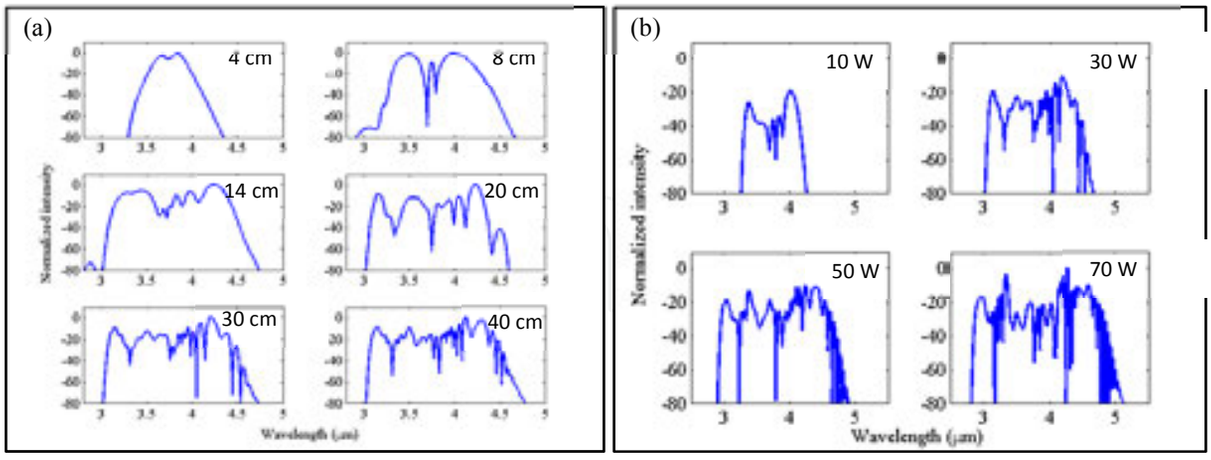


Fig.27 Spectral evolutions for (a) selected propagating distance and (b) peak power

**Figure 27.** Spectral evolutions for (a) selected propagating distance and (b) peak power.

Although the generated mid-SC has a bandwidth of 1.6 μm, it is not enough for drive all the vibraions simultaneously. A feasible approach is to increase the peak power of pump pulse or shorten the pulse duration. Figure 27(b) shows the numerical spectrums for different peak powers after 30 cm propagation with the same pulse duration 200 fs. The input peak powers are 10 W, 30 W, 50 W and 70 W for the top-left, top-right, bottom-left and bottom-right figures respectively. It is clear that the total spectral bandwidth of generated SC is increasing with peak power. And with higher peak power, shorter propagation distance is need to make the spectral broadening to its maximum.

To study the impact of pulse duration on SC generation, peak power of input pulses is kept an constant 30 W in the following simulations. Figure 28(b) exhibit the spectral evolutions for different pulse durations with figures on top-left, top-right, bottom-left, and bottom-right being 100 fs, 200 fs, 300 fs and 500 fs respectively. For pump pulse with shorter duration, the distinct soliton structure is much more clear as in figure (a) and (b) because of a shorter dispersive length $L_D$. They also have a smaller spectral broadening compared with that in figure (c) and (d) due to a lower pulse energy. However, larger input pulse is associated with longer dispersive length, larger pulse energy and higher soliton order which result in a less clear soliton structure and more complex spectral profile in spite of a larger spectral broadening. In the initial propagation, spectral broadening is more with shorter pulse duration because of the larger SPM-induced chirp and its role in FWM.

The spectral broadening with $As_2Se_3$-based PCF is much more than that in silica-glass PCF because of the high nonlinearity. To obtain a continuum with both broad spectral bandwidth and good time structure, a shorter propagation distance is suggested because the weak SSFS effect shifts soliton little towards long-wavelength side with finite propagating distance. And with novel fiber structures, the generated SC has a much larger spectral broadening, such as the mid-infrared SC from 2 to 10 μm by Baili *et al* [118].

length, larger pulse energy and higher soliton order which result in a less clear soliton structure and more complex spectral profile in spite of a larger spectral broadening. In the initial propagation, spectral broadening is more with shorter pulse duration because of the larger SPM-induced chirp and its role in FWM.


http://dx.doi.org/10.5772/59987

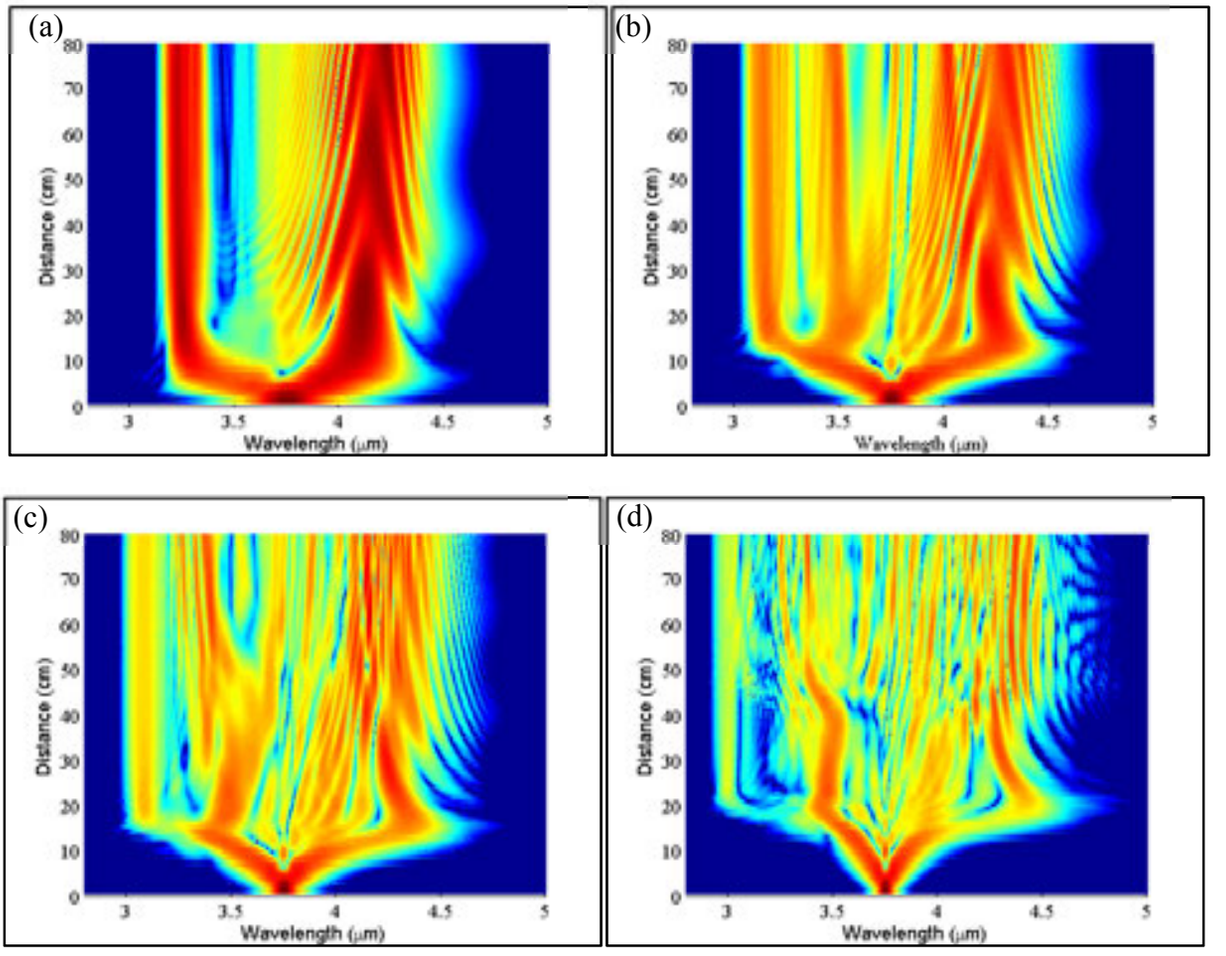


Fig.28 Evolutions over propagation distance for different pulse durations

**Figure 28.** Evolutions over propagation distance for different pulse durations (a) 100 fs; (b) 200 fs; (c) 300 fs; (d) 500 fs

(a) 100 fs; (b) 200 fs; (c) 300 fs; (d) 500 fs

## 5. Conclusions and prospects

The spectral broadening with $As_2Se_3$-based PCF is much more than that in silica-glass PCF because of the high nonlinearity. To obtain a continuum with both broad spectral bandwidth and good time structure, a shorter propagation distance is suggested because the weak SSFS effect shifts soliton little towards long-wavelength side with finite propagating distance. And with novel fiber structures, the generated SC has a much larger spectral broadening, such as the mid-infrared SC from 2 to 10 μm by Baili *et al*.[118]

## 5 Conclusions and prospects

In this chapter, we mainly described the generalized nonlinear Schrödinger equation which is widely used in simulating the pulse evolution in photonic crystal fibers. In this equation, both the higher-order dispersion and nonlinear effects are included, such as self-steepening, optical shock effect and stimulated Raman scattering. The propagation characteristics and the numerical method are introduced to solve the nonlinear Schrödinger equation. Base the equation and numerical method, process of SC generation in a traditional PCF is analyzed in details. Spectral broadening in anomalous dispersions regime is dominated by soliton dynamics, including soliton fission and soliton self-frequency shift, while it is related to SPM effect and optical wave breaking in normal dispersion region. The generated SC has many applications, such as optical frequency metrology, tunable ultrafast fiber laser and nonlinear microscopy for its broad spectrum, high coherence and uniform intensity. Based on the vibrational spectroscopy, CARS microscopy and IR microscopy has been widely used in cellular biology for their label-free and nondestructive imaging. Although the spatial resolution of CARS microscopy is not such high due to the diffraction limit, the APIPD opens up a quite feasible approach to realize nano-scaled imaging. Furthermore, the combination of this CARS nanoscopy and the supercontin-

uum generated in an all-normal dispersion PCF is of crucial importance to study the fine structures and metabolic dynamics in live cells. Besides, combining with atomic force microscope, FTIR microscopy has a spatial resolution below 100nm. This nano-FTIR combing with a mid-infrared supercontinuum source generated from the PCF becoming a powerful tool for chemical identification of unknown nanostructures.

## Author details

Shuanglong Liu, Wei Liu and Hanben Niu*

*Address all correspondence to: hbniu@szu.edu.cn

Key Laboratory of Optoelectronic Devices and Systems of Ministry of Education and Guangdong Province, College of Optoelectronic Engineering, Shenzhen University, Shenzhen, P.R.China

## References

[1] Alfano, R. R.Shapiro, S. L., Emission in the Region 4000 to 7000 Å Via Four-Photon Coupling in Glass, Physical Review Letters, 1970, 24(11): 584-587

[2] Kaiser, P.Astle, H. W., Low-Loss Single-Material Fibers Made From Pure Fused Silica, Bell System Technical Journal, 1974, 53(6): 1021-1039

[3] Knight, J. C., Birks, T. A., Russell, P. S. J. & Atkin, D. M., All-silica single-mode optical fiber with photonic crystal cladding, Opt. Lett., 1996, 21(19): 1547-1549

[4] Russell, P., Photonic crystal fibers, science, 2003, 299(5605): 358-362

[5] Mogilevtsev, D., Birks, T. A. & Russell, P. S. J., Group-velocity dispersion in photonic crystal fibers, Opt. Lett., 1998, 23(21): 1662-1664

[6] Ranka, J. K., Windeler, R. S. & Stentz, A. J., Visible continuum generation in air-silica microstructure optical fibers with anomalous dispersion at 800 nm, Opt. Lett., 2000, 25(1): 25-27

[7] Wadsworth, W. J., Knight, J. C., Ortigosa-Blanch, A., Arriaga, J. *et al.* Soliton effects in photonic crystal fibres at 850 nm. *Electronics Letters* 36, 53-55 (2000).

[8] Liu, X., Xu, C., Knox, W. H., Chandalia, J. K. *et al.*, Soliton self-frequency shift in a short tapered air-silica microstructure fiber, Opt. Lett., 2001, 26(6): 358-360

[9] Husakou, A. V.Herrmann, J., Supercontinuum Generation of Higher-Order Solitons by Fission in Photonic Crystal Fibers, Physical Review Letters, 2001, 87(20): 203901

[10] Washburn, B. R., Ralph, S. E., Lacourt, P. A., Dudley, J. M. *et al.*, Tunable near-infrared femtosecond soliton generation in photonic crystal fibres, ELECTRONICS LETTERS, 2001, 37(25): 1510-1512

[11] Genty, G., Lehtonen, M., Ludvigsen, H., Broeng, J. *et al.*, Spectral broadening of femtosecond pulses into continuum radiation in microstructured fibers, Opt. Express, 2002, 10(20): 1083-1098

[12] Avdokhin, A. V., Popov, S. V. & Taylor, J. R., Continuous-wave, high-power, Raman continuum generation in holey fibers, Opt. Lett., 2003, 28(15): 1353-1355

[13] Dudley, J. M., Genty, G. & Coen, S., Supercontinuum generation in photonic crystal fiber, Reviews of Modern Physics, 2006, 78(4): 1135-1184

[14] Wisse, E., De Zanger, R., Jacobs, R. & McCuskey, R., Scanning electron microscope observations on the structure of portal veins, sinusoids and central veins in rat liver, Scanning electron microscopy, 1982, Pt 3): 1441-1452

[15] Binnig, G.Rohrer, H., Scanning tunneling microscopy, Surface Science, 1983, 126(1): 236-244

[16] Binnig, G., Gerber, C., Stoll, E., Albrecht, T. *et al.*, Atomic resolution with atomic force microscope, EPL (Europhysics Letters), 1987, 3(12): 1281

[17] Juhun, P., Jinwoo, L., Seon, N., Kwang, H. *et al.*, Sub-Diffraction Limit Imaging of Inorganic Nanowire Networks Interfacing Cells, Small, 2014, 10(3): 462-468

[18] Hess Samuel T, G. T. P. K., Mason Michael D, Ultra-High Resolution Imaging by Fluorescence Photoactivation Localization Microscopy, Biophysical Journal, 2006, 91(11): 4258-4272

[19] Michael J Rust, M. B., Xiaowei Zhuang, Sub-diffraction-limit imaging by stochastic optical reconstruction microscopy (STORM), Nature Methods, 2006, 3(10): 47

[20] Hell Stefan W, W. J., Breaking the diffraction resolution limit by stimulated emission: stimulated-emission-depletion fluorescence microscopy, Opt. Lett., 1994, 19(11): 780-782

[21] Wu, J., Cohen, L. & Mason, W., Fluorescent and luminescent probes for biological activity, London: Academic, 1993,

[22] Evans, C. L.Xie, X. S., Coherent Anti-Stokes Raman Scattering Microscopy: Chemical Imaging for Biology and Medicine, Annual Review of Analytical Chemistry, 2008, 1(1): 883-909

[23] Yuan, J.-H., Xiao, F.-R., Wang, G.-Y. & Xu, Z.-Z., Imaging properties of coherent anti-Stokes Raman scattering microscope, Chinese Physics, 2005, 14(935-941

[24] Xia, L., Hui, Z., Xiang-Yun, Z., Shi-An, Z. *et al.*, Experimental Investigation on Selective Excitation of Two-Pulse Coherent Anti-Stokes Raman Scattering, Chinese Physics Letters, 2008, 25(6): 2062

[25] Liu Wei, N. H., Diffraction barrier breakthrough in coherent anti-Stokes Raman scattering microscopy by additional probe-beam-induced phonon depletion, Physical Review A, 2011, 83(2): 023830

[26] Sage, J. T., Zhang, Y., McGeehan, J., Ravelli, R. B. G. *et al.*, Infrared protein crystallography, Biochimica et Biophysica Acta (BBA) - Proteins and Proteomics, 2011, 1814(6): 760-777

[27] Gillie, J. K.Hochlowski, J., Infrared Spectroscopy, Analytical Chemistry, 2000, 75(12):

[28] Huth, F., Schnell, M., Wittborn, J., Ocelic, N. *et al.*, Infrared-spectroscopic nanoimaging with a thermal source, Nature materials, 2011, 10(5): 352-356

[29] Reffner, J. A., Martoglio, P. A. & Williams, G. P., Fourier transform infrared microscopical analysis with synchrotron radiation: the microscope optics and system performance, Review of Scientific Instruments, 1995, 66(2): 1298-1302

[30] Tobin, M. J., Chesters, M. A., Chalmers, J. M., Rutten, F. J. *et al.*, Infrared microscopy of epithelial cancer cells in whole tissues and in tissue culture, using synchrotron radiation, Faraday discussions, 2004, 126(27-39

[31] Kumar, V., George, A., Knight, J. & Russell, P., Tellurite photonic crystal fiber, Opt. Express, 2003, 11(20): 2641-2645

[32] Sanghera, J. S., Shaw, L. B. & Aggarwal, I. D., Applications of chalcogenide glass optical fibers, Comptes Rendus Chimie, 2002, 5(12): 873-883

[33] Xia, C., Kumar, M., Kulkarni, O. P., Islam, M. N. *et al.*, Mid-infrared supercontinuum generation to 4.5 μm in ZBLAN fluoride fibers by nanosecond diode pumping, Opt. Lett., 2006, 31(17): 2553-2555

[34] Diament, P. *Wave transmission and fiber optics*. Vol. 74 (Macmillan, 1990).

[35] Blow, K. J.Wood, D., Theoretical description of transient stimulated Raman scattering in optical fibers, Quantum Electronics, IEEE Journal of, 1989, 25(12): 2665-2673

[36] Karasawa, N., Nakamura, S., Nakagawa, N., Shibata, M. *et al.*, Comparison between theory and experiment of nonlinear propagation for a-few-cycle and ultrabroadband optical pulses in a fused-silica fiber, Quantum Electronics, IEEE Journal of, 2001, 37(3): 398-404

[37] Kibler, B., Dudley, J. M. & Coen, S., Supercontinuum generation and nonlinear pulse propagation in photonic crystal fiber: influence of the frequency-dependent effective mode area, Appl. Phys. B, 2005, 81(2-3): 337-342

[38] Mamyshev, P. V.Chernikov, S. V., Ultrashort-pulse propagation in optical fibers, Opt. Lett., 1990, 15(19): 1076-1078

[39] Chernikov, S. V.Mamyshev, P. V., Femtosecond soliton propagation in fibers with slowly decreasing dispersion, J. Opt. Soc. Am. B, 1991, 8(8): 1633-1641

[40] Stolen, R. H.Tomlinson, W. J., Effect of the Raman part of the nonlinear refractive index on propagation of ultrashort optical pulses in fibers, J. Opt. Soc. Am. B, 1992, 9(4): 565-573

[41] Lin, Q.Agrawal, G. P., Raman response function for silica fibers, Opt. Lett., 2006, 31(21): 3086-3088

[42] Hollenbeck, D.Cantrell, C. D., Multiple-vibrational-mode model for fiber-optic Raman gain spectrum and response function, J. Opt. Soc. Am. B, 2002, 19(12): 2886-2892

[43] Xueming, L.Byoungho, L., A fast method for nonlinear Schrodinger equation, Photonics Technology Letters, IEEE, 2003, 15(11): 1549-1551

[44] Reid, D. T., Loza-Alvarez, P., Brown, C. T. A., Beddard, T. *et al.*, Amplitude and phase measurement of mid-infrared femtosecond pulses by using cross-correlation frequency-resolved optical gating, Opt. Lett., 2000, 25(19): 1478-1480

[45] Linden, S., Kuhl, J. & Giessen, H., Amplitude and phase characterization of weak blue ultrashort pulses by downconversion, Opt. Lett., 1999, 24(8): 569-571

[46] Dudley, J., Gu, X., Xu, L., Kimmel, M. *et al.*, Cross-correlation frequency resolved optical gating analysis of broadband continuum generation in photonic crystal fiber: simulations and experiments, Opt. Express, 2002, 10(21): 1215-1221

[47] Kane, D. J.Trebino, R., Single-shot measurement of the intensity and phase of an arbitrary ultrashort pulse by using frequency-resolved optical gating, Opt. Lett., 1993, 18(10): 823-825

[48] Trebino, R., DeLong, K. W., Fittinghoff, D. N., Sweetser, J. N. *et al.*, Measuring ultrashort laser pulses in the time-frequency domain using frequency-resolved optical gating, Review of Scientific Instruments, 1997, 68(9): 3277-3295

[49] Tatian, B., Fitting refractive-index data with the Sellmeier dispersion formula, Appl. Opt., 1984, 23(24): 4477-4485

[50] Adams, M., An introduction to optical waveguides, Chichester-New York, 1981,

[51] Malitson, I. H., Interspecimen Comparison of the Refractive Index of Fused Silica, J. Opt. Soc. Am., 1965, 55(10): 1205-1208

[52] Cucinotta, A., Selleri, S., Vincetti, L. & Zoboli, M., Holey fiber analysis through the finite-element method, Photonics Technology Letters, IEEE, 2002, 14(11): 1530-1532

[53] Koshiba, M., Full-vector analysis of photonic crystal fibers using the finite element method, IEICE transactions on electronics, 2002, 85(4): 881-888

[54] Brechet, F., Marcou, J., Pagnoux, D. & Roy, P., Complete analysis of the characteristics of propagation into photonic crystal fibers, by the finite element method, Optical Fiber Technology, 2000, 6(2): 181-191

[55] Shibata, N., Braun, R. & Waarts, R., Phase-mismatch dependence of efficiency of wave generation through four-wave mixing in a single-mode optical fiber, Quantum Electronics, IEEE Journal of, 1987, 23(7): 1205-1210

[56] Cristiani, I., Tediosi, R., Tartara, L. & Degiorgio, V., Dispersive wave generation by solitons in microstructured optical fibers, Opt. Express, 2004, 12(1): 124-135

[57] Cheng, J.-X., Jia, Y. K., Zheng, G. & Xie, X. S., Laser-Scanning Coherent Anti-Stokes Raman Scattering Microscopy and Applications to Cell Biology, Biophysical Journal, 2002, 83(1): 502-509

[58] Cheng, J.-X.Xie, X. S., Coherent Anti-Stokes Raman Scattering Microscopy: Instrumentation, Theory, and Applications, The Journal of Physical Chemistry B, 2003, 108(3): 827-840

[59] Horie, K., Ushiki, H. & Winnik, F. M., The Interaction of Light with Materials II, Molecular Photonics: Fundamentals and Practical Aspects, 177-199

[60] Vallée, F.Bogani, F., Coherent time-resolved investigation of LO-phonon dynamics in GaAs, Physical Review B, 1991, 43(14): 12049

[61] Waltner, P., Materny, A. & Kiefer, W., Phonon relaxation in CdSSe semiconductor quantum dots studied by femtosecond time-resolved coherent anti-Stokes Raman scattering, Journal of Applied Physics, 2000, 88(9): 5268-5271

[62] Penzkofer, A., Laubereau, A. & Kaiser, W., High intensity Raman interactions, Progress in Quantum Electronics, 1979, 6(2): 55-140

[63] Loudon, R. *The quantum theory of light*. (Oxford university press, 2000).

[64] El-Diasty, F., Coherent anti-Stokes Raman scattering: Spectroscopy and microscopy, Vibrational Spectroscopy, 2011, 55(1): 1-37

[65] Portnov, A., Rosenwaks, S. & Bar, I., Detection of particles of explosives via backward coherent anti-Stokes Raman spectroscopy, Applied Physics Letters, 2008, 93(4): -

[66] Begley, R. F., Harvey, A. B. & Byer, R. L., Coherent anti-Stokes Raman spectroscopy, Applied Physics Letters, 1974, 25(7): 387-390

[67] Cui, M., Bachler, B. R. & Ogilvie, J. P., Comparing coherent and spontaneous Raman scattering under biological imaging conditions, Opt. Lett., 2009, 34(6): 773-775

[68] Zumbusch, A., Holtom, G. R. & Xie, X. S., Three-Dimensional Vibrational Imaging by Coherent Anti-Stokes Raman Scattering, Physical Review Letters, 1999, 82(20): 4142-4145

[69] Bergner, G., Chatzipapadopoulos, S., Akimov, D., Dietzek, B. *et al.*, Quantitative CARS Microscopic Detection of Analytes and Their Isotopomers in a Two-Channel Microfluidic Chip, Small, 2009, 5(24): 2816-2818

[70] Bergner, G., Albert, C. R., Schiller, M., Bringmann, G. *et al.*, Quantitative detection of C-deuterated drugs by CARS microscopy and Raman microspectroscopy, Analyst, 2011, 136(18): 3686-3693

[71] Zimmerley, M., Lin, C.-Y., Oertel, D. C., Marsh, J. M. *et al.*, Quantitative detection of chemical compounds in human hair with coherent anti-Stokes Raman scattering microscopy, BIOMEDO, 2009, 14(4): 044019-044019-044017

[72] Beeker, W. P., Groß, P., Lee, C. J., Cleff, C. *et al.*, A route to sub-diffraction-limited ? CARS Microscopy, Opt. Express, 2009, 17(25): 22632-22638

[73] Nikolaenko, A., Krishnamachari, V. V. & Potma, E. O., Interferometric switching of coherent anti-Stokes Raman scattering signals in microscopy, Physical Review A, 2009, 79(1): 013823

[74] Beeker, W. P., Lee, C. J., Boller, K.-J., Groß, P. *et al.*, Spatially dependent Rabi oscillations: An approach to sub-diffraction-limited coherent anti-Stokes Raman-scattering microscopy, Physical Review A, 2010, 81(1): 012507

[75] Tada, K.Karasawa, N., Broadband coherent anti-Stokes Raman scattering spectroscopy using soliton pulse trains from a photonic crystal fiber, Optics Communications, 2009, 282(19): 3948-3952

[76] Sidorov-Biryukov, D. A., Serebryannikov, E. E. & Zheltikov, A. M., Time-resolved coherent anti-Stokes Raman scattering with a femtosecond soliton output of a photonic-crystal fiber, Opt. Lett., 2006, 31(15): 2323-2325

[77] Paulsen, H. N., Hilligse, K. M., Thøgersen, J., Keiding, S. R. *et al.*, Coherent anti-Stokes Raman scattering microscopy with a photonic crystal fiber based light source, Opt. Lett., 2003, 28(13): 1123-1125

[78] Beaud, P., Hodel, W., Zysset, B. & Weber, H., Ultrashort pulse propagation, pulse breakup, and fundamental soliton formation in a single-mode optical fiber, Quantum Electronics, IEEE Journal of, 1987, 23(11): 1938-1946

[79] Aitchison, J., Weiner, A., Silberberg, Y., Oliver, M. *et al.*, Observation of spatial optical solitons in a nonlinear glass waveguide, Opt. Lett., 1990, 15(9): 471-473

[80] Gordon, J. P., Theory of the soliton self-frequency shift, Opt. Lett., 1986, 11(10): 662-664

[81] Mitschke, F. M.Mollenauer, L. F., Discovery of the soliton self-frequency shift, Opt. Lett., 1986, 11(10): 659-661

[82] Hooper, L. E., Mosley, P. J., Muir, A. C., Wadsworth, W. J. *et al.* in *Conference on Lasers and Electro-Optics*. CTuX4 (Optical Society of America).

[83] Hooper, L. E., Mosley, P. J., Muir, A. C., Wadsworth, W. J. *et al.*, Coherent supercontinuum generation in photonic crystal fiber with all-normal group velocity dispersion, Opt. Express, 2011, 19(6): 4902-4907

[84] Hartung, A., Heidt, A. M. & Bartelt, H., Design of all-normal dispersion microstructured optical fibers for pulse-preserving supercontinuum generation, Opt. Express, 2011, 19(8): 7742-7749

[85] Tomlinson, W., Stolen, R. H. & Johnson, A. M., Optical wave breaking of pulses in nonlinear optical fibers, Opt. Lett., 1985, 10(9): 457-459

[86] Dorrer, C., Salin, F., Verluise, F. & Huignard, J., Programmable phase control of femtosecond pulses by use of a nonpixelated spatial light modulator, Opt. Lett., 1998, 23(9): 709-711

[87] Karasawa, N., Li, L., Suguro, A., Shigekawa, H. *et al.*, Optical pulse compression to 5.0 fs by use of only a spatial light modulator for phase compensation, JOSA B, 2001, 18(11): 1742-1746

[88] Knoll, B.Keilmann, F., Near-field probing of vibrational absorption for chemical microscopy, Nature, 1999, 399(6732): 134-137

[89] Chabal, Y. J., Surface infrared spectroscopy, Surface Science Reports, 1988, 8(5): 211-357

[90] Conley, R. T. *Infrared spectroscopy*. (Allyn and Bacon, 1972).

[91] Chappell, J., Bloch, A., Bryden, W., Maxfield, M. *et al.*, Degree of charge transfer in organic conductors by infrared absorption spectroscopy, Journal of the American Chemical Society, 1981, 103(9): 2442-2443

[92] Zhu, X., Suhr, H. & Shen, Y., Surface vibrational spectroscopy by infrared-visible sum frequency generation, Physical Review B, 1987, 35(6): 3047

[93] Kahn, A. H., Theory of the infrared absorption of carriers in germanium and silicon, Physical Review, 1955, 97(6): 1647

[94] Iwata, K.Hamaguchi, H.-O., Construction of a Versatile Microsecond Time-Resolved Infrared Spectrometer, Appl. Spectrosc., 1990, 44(9): 1431-1437

[95] VAN DE WEERT, M., Fourier Transform Infrared, Methods for Structural Analysis of Protein Pharmaceuticals, 2005, 3(131

[96] Rochow, T. G.Tucker, P. A. in *Introduction to Microscopy by Means of Light, Electrons, X Rays, or Acoustics* 257-264 (Springer, 1994).

[97] Arrondo, J. L. R., Muga, A., Castresana, J. & Goñi, F. M., Quantitative studies of the structure of proteins in solution by Fourier-transform infrared spectroscopy, Progress in biophysics and molecular biology, 1993, 59(1): 23-56

[98] Helm, D., Labischinski, H., Schallehn, G. & Naumann, D., Classification and identification of bacteria by Fourier-transform infrared spectroscopy, Journal of general microbiology, 1991, 137(1): 69-79

[99] Pasquini, C., Near infrared spectroscopy: fundamentals, practical aspects and analytical applications, Journal of the Brazilian Chemical Society, 2003, 14(2): 198-219

[100] Gagel, J. J.Biemann, K., Continuous recording of reflection-absorbance Fourier transform infrared spectra of the effluent of a microbore liquid chromatograph, Analytical chemistry, 1986, 58(11): 2184-2189

[101] Buican, T. N.Carrieri, A. H. Ultra-high speed solid-state FTIR spectroscopy and applications for chemical defense. (DTIC Document, 2004).

[102] Schmitt, J.Flemming, H.-C., FTIR-spectroscopy in microbial and material analysis, International Biodeterioration & Biodegradation, 1998, 41(1): 1-11

[103] Pandey, K., A study of chemical structure of soft and hardwood and wood polymers by FTIR spectroscopy, Journal of Applied Polymer Science, 1999, 71(12): 1969-1975

[104] Meilunas, R. J., Bentsen, J. G. & Steinberg, A., Analysis of aged paint binders by FTIR spectroscopy, Studies in conservation, 1990, 35(1): 33-51

[105] Carr, G., Resolution limits for infrared microspectroscopy explored with synchrotron radiation, Review of Scientific Instruments, 2001, 72(3): 1613-1619

[106] Knoll, B.Keilmann, F., Enhanced dielectric contrast in scattering-type scanning near-field optical microscopy, Optics communications, 2000, 182(4): 321-328

[107] Hillenbrand, R., Knoll, B. & Keilmann, F., Pure optical contrast in scattering-type scanning near-field microscopy, Journal of microscopy, 2001, 202(1): 77-83

[108] Dazzi, A., Prazeres, R., Glotin, F. & Ortega, J. M., Local infrared microspectroscopy with subwavelength spatial resolution with an atomic force microscope tip used as a photothermal sensor, Opt. Lett., 2005, 30(18): 2388-2390

[109] Dazzi, A., Prazeres, R., Glotin, F. & Ortega, J., Subwavelength infrared spectromicroscopy using an AFM as a local absorption sensor, Infrared physics & technology, 2006, 49(1): 113-121

[110] Dazzi, A., Prazeres, R., Glotin, F. & Ortega, J., Analysis of nano-chemical mapping performed by an AFM-based ("AFMIR") acousto-optic technique, Ultramicroscopy, 2007, 107(12): 1194-1200

[111] Holman, H. Y. N., Martin, M. C., Blakely, E. A., Bjornstad, K. *et al.*, IR spectroscopic characteristics of cell cycle and cell death probed by synchrotron radiation based Fourier transform IR spectromicroscopy, Biopolymers, 2000, 57(6): 329-335

[112] Yuan, W., Coherent broadband mid-infrared supercontinuum generation in As2Se3 photonic crystal fiber, arXiv preprint arXiv:1309.5830, 2013,

[113] Shaw, L., Thielen, P., Kung, F., Nguyen, V. *et al.* in *Conf. Adv. Solid State Lasers (ASSL), Seattle, WA.*

[114] Price, J. H. V., Feng, X., Heidt, A. M., Brambilla, G. *et al.*, Supercontinuum generation in non-silica fibers, Optical Fiber Technology, 2012, 18(5): 327-344

[115] Kubat, I., Agger, C. S., Moselund, P. M. & Bang, O., Mid-infrared supercontinuum generation to 4.5 μm in uniform and tapered ZBLAN step-index fibers by direct pumping at 1064 or 1550 nm, JOSA B, 2013, 30(10): 2743-2757

[116] Granzow, N., Stark, S. P., Schmidt, M. A., Tverjanovich, A. *et al.*, Supercontinuum generation in chalcogenide-silica step-index fibers, Opt. Express, 2011, 19(21): 21003-21010

[117] Baili, A., Cherif, R., Saini, T. S., Kumar, A. *et al.* 92000S-92000S-92006.

[118] Ung, B.Skorobogatiy, M., Chalcogenide microporous fibers for linear and nonlinear applications in the mid-infrared, Opt. Express, 2010, 18(8): 8647-8659

[119] Hu, J., Menyuk, C. R., Shaw, L. B., Sanghera, J. S. *et al.* in *Lasers and Electro-Optics, 2008 and 2008 Conference on Quantu*m Electronics and Laser Science. CLEO/QELS 2008. Conference on. 1-2 (IET).